The Effect of the Variable Chaplygin Gas on the CMB

Sphesihle Makhathini

University of KwaZulu-Natal

School of Physics and Chemistry

Supervisor : Dr. Caroline Zunckel

A Thesis submitted in part fulfilment of the degree of MSc in Physics
at the
University of KwaZulu-Natal 2013

As the candidate's supervisor I have approved this dissertation for submission:
Signed :_____ Name:___Caroline Zunckel_____ Date___25 April 2013___

Declaration

I, *Sphesihle Makhathini*, declare that

- The research reported in this dissertation, except where otherwise indicated, is my original research.

- This dissertation has not been submitted for any degree or examination at any other university.

- This dissertation does not contain other persons data, pictures, graphs or other information, unless specifically acknowledged as being sourced from other persons.

- This dissertation does not contain other persons' writing, unless specifically acknowledged as being sourced from other researchers.

- This dissertation does not contain text, graphics or tables copied and pasted from the Internet, unless specifically acknowledged, and the source being detailed in the dissertation and in the References sections.

Signed :

Abstract

In this dissertation, we consider the variable chaplygin gas (VCG) model as derived from the Tachyon gas model and search for a sub-class of models that provide an adequate fit to the cosmic microwave background (CMB) observations. We find that, for an appropriate choice of VCG parameters, up to $\sim 80\%$ of the VCG collapses into a gravitationally bound condensate which behaves as matter; the evolution of the remaining VCG, as governed by its equation of state, brings about accelerated expansion at late times. In light of this high collapsed fraction, we approximate the VCG transfer function with that of cold dark matter. We show that we can sufficiently describe the VCG cosmology from decoupling to today in terms of a model in which the gravitationally bound condensate plays the role of cold dark matter and the remaining VCG takes the place of dark energy in the concordance model. We then compute the CMB temperature anisotropy spectrum for a subset of VCG models and proceed to find a best-fit model to the WMAP-9yr data [46]. Our best-fit model has a χ^2 per degrees of freedom of 2.03.

Acknowledgements

Contents

Chapter 1

Introduction

With the advances in observational and theoretical cosmology, in recent years, questions about the age, geometry, dynamics, content, and the origin of the structure in the universe can be answered quantitatively with reasonable confidence. We know that the very early universe was in an extremely hot state which expanded rapidly, causing it to cool, and resulting in the present expanding state. Current cosmological observations suggest that we live in an almost spatially flat, expanding universe with about 70% percent of the energy density attributed to a component with negative pressure, dubbed *dark energy*. The remainder of the energy density is attributed to 25% non-baryonic matter, known as dark matter, and about 5% baryonic matter.

This cosmological model is known as the ΛCDM model. The ΛCDM model supposes that dark energy is Einstein's cosmological constant, while dark matter particles are assumed to non-relativistic, cold dark matter (CDM). However, despite the consistency with most observations, the ΛCDM model has encountered some theoretical problems [54]. Furthermore, neither dark matter nor dark energy has been directly detected. This leaves the door open to the possibility that dark matter and dark energy are manifestations of the same cosmic fluid. This scenario, where dark matter and dark energy are manifestations of the same cosmic fluid is called *Quartessence*. In light of the challenges facing ΛCDM it is important to explore such a scenario.

In this dissertation, we investigate the possibility of a quartessence model known as the *variable Chaplygin gas* (VCG) as a viable alternate cosmology to ΛCDM in light of the current observational data.

In this introduction we first describe the theory that governs the dynamics of the universe. Then we give a description of the current cosmological observations and how these observations have led to the current concordance model. Most of this background material is based on references [1, 2, 3]. Finally we present quartessence as a possible alternative to ΛCDM.

1.1   Describing the Universe

In this section we present a qualitative description of the theoretical framework that describes the dynamics of our universe.

1.1.1 Equations of Motion

The universe is believed to be isotropic and homogeneous, the so-called *cosmological principle.* Isotropy means that the universe looks the same in every direction, which then implies that observations made in one direction are a sufficient test of cosmology. Isotropy is in very good agreement with observations (0.001% accuracy). Homogeneity means the general picture of the universe as a function of time is independent of the position of the observer. The assertion of the cosmological principle together with General Relativity describes our universe. General Relativity relates the metric, which describes gravitation, to the energy in the universe through the Einstein equations, which determine the dynamics of the universe:

$$G_{\mu\nu} = R_{\mu\nu} - \frac{1}{2}g_{\mu\nu}R = 8\pi G T_{\mu\nu}, \tag{1.1}$$

where $G_{\mu\nu}$ is the Einstein tensor; $R_{\mu\nu}$ is the Ricci tensor, which depends on the metric derivatives; the Ricci scalar R is a contraction of the Ricci tensor, $R = g^{\mu\nu}R_{\mu\nu}$; G is Newton's gravitational constant; and $T_{\mu\nu}$ is the energy-momentum tensor. The metric, $g_{\mu\nu}$, which describes a smooth expanding universe is the Friedman-Lemaitre-Robertson-Walker (FRW) metric

$$ds^2 = dt^2 - a(t)[dr^2 + S_\kappa(r)^2 d\Omega^2], \tag{1.2}$$

where $a(t)$ is the scale factor. It is conventional to set its value today to unity and its value at the Big Bang to be zero; $d\Omega^2 = d\theta^2 + \sin^2(\theta)d\phi^2$ and

$$S_\kappa = \left\{ \begin{array}{ll} \frac{1}{\kappa}\sin(r\sqrt{\kappa}) & \text{for } \kappa > 0 \\ r & \kappa = 0 \\ \frac{1}{\kappa}\sinh(r\sqrt{\kappa}) & \text{for } \kappa < 0 \end{array} \right\}. \tag{1.3}$$

Here, κ denotes the curvature of the universe and can be either positive, zero or negative depending on the geometry of the universe. A flat universe is Euclidean and has zero curvature: particles remain parallel as long as they travel freely. In an open universe which has negative curvature, particles which start out parallel gradually diverge as they travel freely. In a closed universe, which has positive curvature; particles which start out parallel gradually converge as they travel freely.

The left hand side of (1.1) is a function of the metric and the right a function of the energy. Assuming each component in the universe has an energy density ρ_i and pressure p_i, the total energy density and pressure are given by

$$\rho = \sum_i \rho_i \tag{1.4}$$

$$p = \sum_i p_i, \tag{1.5}$$

respectively. For a perfect isotropic fluid the energy-momentum tensor is given by

$$T^\mu{}_\nu = \begin{pmatrix} -\rho & 0 & 0 & 0 \\ 0 & p & 0 & 0 \\ 0 & 0 & p & 0 \\ 0 & 0 & 0 & p \end{pmatrix}, \tag{1.6}$$

where p is the pressure of the fluid with energy density ρ. For a perfect fluid energy conservation requires

$$T^{\mu\nu}{}_{;\mu} = 0, \tag{1.7}$$

which yields as its longitudinal part the continuity equation

$$\frac{\partial\rho}{\partial t} + 3\frac{\dot{a}}{a}(\rho + p) = 0. \tag{1.8}$$

The continuity equation can then be integrated to get the evolution of the energy density for each component as

$$\rho_i \propto \exp\left\{-3\int^a \frac{da}{a}[1 + w_i(a)]\right\} \tag{1.9}$$

where $w_i(a)$ is the equation of state parameter, defined as

$$w_i = \frac{p_i}{\rho_i}. \tag{1.10}$$

Knowing the equation of state parameter for a given component in the universe, the energy density evolution of each component can be obtained using Equation (1.9). The Einstein equations yields the evolution of $\dot{a}$ as

$$-\left(\frac{\dot{a}}{a}\right)^2 + \frac{8\pi G}{3}\rho + \frac{\kappa}{a^2} = 0, \tag{1.11}$$

and $\ddot{a}$ is given by

$$\frac{\ddot{a}}{a} + \frac{4\pi G}{3}(\rho + 3p) = 0. \tag{1.12}$$

Therefore, for a universe containing fluids with known equation of state parameters w_i, the dynamics are described by equations (1.9),(1.11) and (1.12). Equation (1.11) is known as the Friedman equation. To quantify the change in the scale factor and its relation to the energy, it is useful to define the Hubble parameter,

$$H = \frac{1}{a}\frac{da}{dt} = \frac{\dot{a}}{a}. \tag{1.13}$$

Now the Friedman equation can be written using the Hubble parameter as

$$-H^2 + \frac{8\pi G}{3}\rho + \frac{\kappa}{a^2} = 0. \tag{1.14}$$

Another quantity that is frequently used in cosmology is the redshift, which is defined as the ratio of the wavelength when light was observed and light was emitted, i.e,

$$z + 1 = \frac{\lambda_{\text{observed}}}{\lambda_{\text{emitted}}} = \frac{1}{a}. \tag{1.15}$$

Redshift is often used as a time and distance parameter in cosmology. The redshift of the light emitted by source at time t_i, $z_i = a(t)^{-1}$, gives the size of the universe at the time t_i.

1.2 Evidence for the Big Bang Model

In this section we describe the current cosmological observations. In this description we highlight the role each these observations play in validating the Big Bang Model. We then proceed to study how these observations have led to the current concordance model universe.

1.2.1 The Hubble Expansion

One giant leap in understanding the dynamics of the universe was Edwin Hubble's discovery that the universe is expanding. Using the 100-inch Hooker telescope at Mount Wilkinson Observatory Hubble measured distances to galaxies by isolating individual Cepheids in those galaxies. Cepheids are stars which pulsate. The period of their pulsation is related to their intrinsic brightness. Cepheids with same period have the same intrinsic luminosity. Distances to these objects can be inferred by finding the correlation between their true and observed brightness. Hubble combined his measurements with Veto Slipher's redshift measurements for the galaxies, which may be determined by measuring the shifts of spectral lines in spectra from galaxies. He found that *galaxy redshifts were proportional to galaxy distances*, and concluded that these galaxies were receding from us with a velocity proportional to their distance from us. According to the cosmological principle we hold no special place in the universe, therefore it must be that galaxies recede from each other with a velocity v, proportional to the distance, r, between them. This relation is known as the Hubble law:

$$v = H_0 r. \tag{1.16}$$

The constant H_0 is referred to as the Hubble constant and is a measure of the rate of the recession. Present measures of the Hubble rate are parametrised by h, defined via,

$$H_0 = 100h \text{ km s}^{-1} \text{ Mpc}^{-1}. \tag{1.17}$$

The Hubble law remains one of most compelling pieces of evidence that the universe is expanding, which is consistent with the Big Bang model. Therefore accurate measurement of the expansion rate is paramount. The standard candles that are used today are Type Ia supernovae (SN1a), being much brighter than Cepheids they can extend the Hubble diagram 1.1a to very large redshifts 1.1b, and measure the expansion rate to a very high accuracy. very
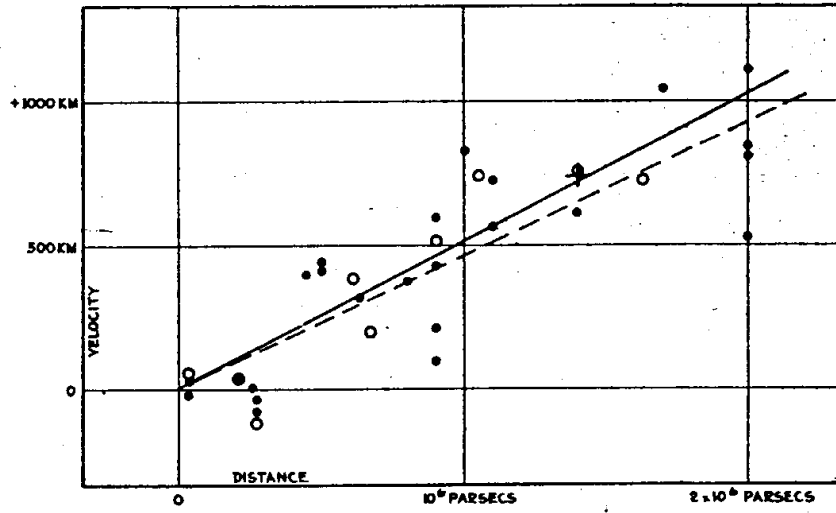
(a) The original Hubble diagram, showing the velocities of galaxies vs distance, taken from [4]. The solid line is the line of best-fit for data points (filled) corrected for the motion of the sun, while the dashed line is the best-fit for the uncorrected data points (unfilled).
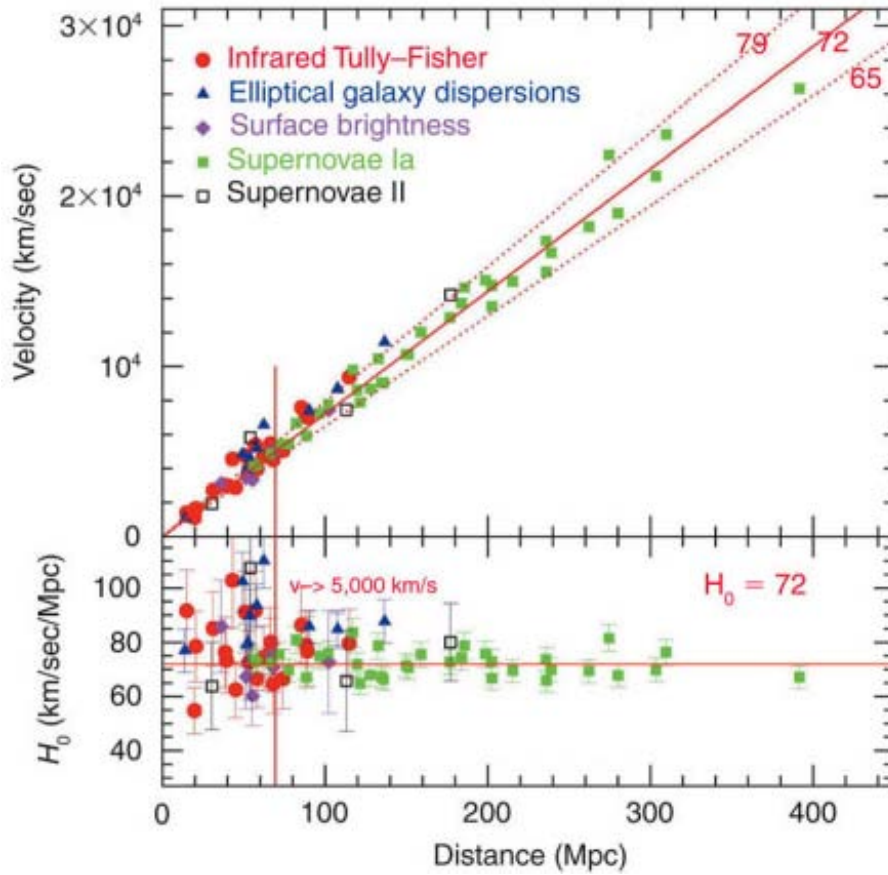
(b) Hubble Diagram from the Hubble Space Telescope Key Project [5], constructed from five different distance measures. The horizon lines give the best-fit value of $H_0 = 72 \pm 8 \mathrm{km\ s^{-1} Mpc^{-1}}$.

Figure 1.1

1.2.2 Light Element Abundance

The abundance of elements in the universe provides one of the most compelling pieces of evidence in support of the Big Bang model. Historically it was assumed that all stars began their life comprised entirely of hydrogen, with heavier elements being generated via nuclear fusion reactions at their cores. While this is the process giving rise to heavy elements, it is now established that not all the light elements– deuterium, helium-3, lithium, and especially helium-4, could have been created in this manner. In fact the spectra of very young stars indicates these approach non-zero abundances. In particular, the measurement of primordial deuterium pins down the baryon density extremely accurately to only a few percent of the critical density.
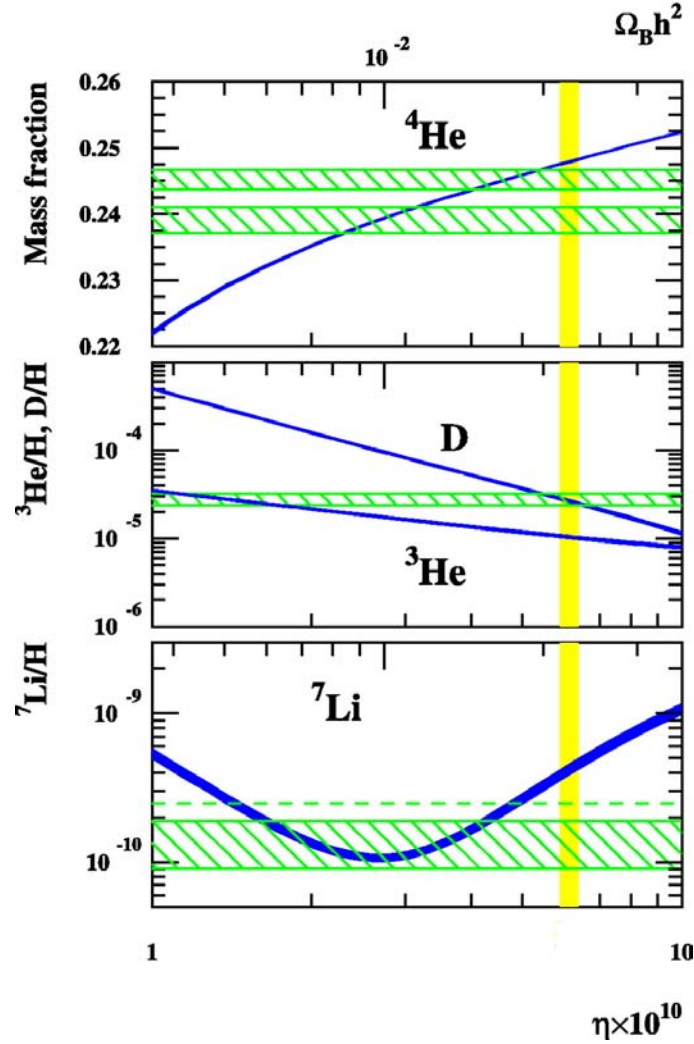

Figure 1.2: Constraints on the baryon density as predicted by BBN taken from [6]. The curves show the primordial abundances of deuterium, helium-3, lithium and helium-4 as predicted by the standard model of the BBN, as function of baryon density-photon ratio. The boxes show the observed abundances.

When the universe was much hotter and denser, when the temperature was of order ~ 10 MeV, there were no neutral atoms or even bound nuclei. The vast amounts of radiation in such a hot environment ensured that any atom or nucleus produced would be immediately destroyed by a high energy photon. However, according to the Big Bang model, as the universe cooled well below binding energies of typical nuclei (~ 1MeV), the production of light elements could take place. This period when neutral nuclei began to form is referred to as the *recombination epoch*. Knowing the conditions of the early universe and the relevant nuclear cross-sections (standard model of particle physics), one can predict the expected primordial abundances of Li, He and D in this model. This synthesis of light elements is known as Big Bang Nucleosythesis (BBN). The predictions of BBN are in very good agreement with the current estimates of light element predictions, and this consistency sets the Big Bang model on an even firmer footing. The combined proton-neutron density is called the baryon density since both protons and neutrons have baryon number one and these are the only baryons around at these early times. Thus BBN may be used to measure the baryon density in the universe (see section 1.3).

1.2.3   Cosmic Microwave Background

During the epoch of recombination, photons are coupled to baryons. Cosmic expansion causes the baryon density to decrease causing a decrease in photon-baryon interaction. When the photon-baryon interaction rate decreases below the cosmic expansion rate, the photons are decoupled from the baryons and begin to free-stream. George Gamow in 1948 predicted that this primordial radiation should be present today with an almost perfect uniformity everywhere in the universe. In the early 1960s this primordial radiation was recognised by Robert Dicke and Yakov Zeldovich as a detectable phenomenon.
In 1965, Arno Penzias and Robert Wilson at the Bell Telephone Laboratories in New Jersey were measuring sky brightness at radio wavelengths. Their measurements had an excess of 3.5 K which they could not account for. When Penzias and Wilson heard of Dicke's work they realised they had detected the CMB. In 1990 satellite measurements confirmed the CMB has a blackbody spectral distribution with an apparent temperature of 2.7 K. As a result of the continual expansion of the universe, this radiation has been stretched out to longer wavelengths which today exist in the microwave region of the electromagnetic spectrum. Due to its near perfect uniformity, we conclude that this radiation originated in a time when the universe was much smaller, hotter, and denser.

1.3   Cosmic Budget

One major goal in observational cosmology is to know the precisely the fraction contribution of each component of the universe. Observations and theory point to a universe made up of radiation, ρ_γ, baryonic matter (electrons, neutrons, protons), ρ_b, dark matter, ρ_{dm}, dark energy, ρ_{de} and neutrinos ρ_{nu}. In this section we calculate the contribution of each of the above mentioned species to the energy density of the universe. Before we proceed we need to define *the critical density*. Note that in a

flat universe ($\kappa = 0$) the Friedman equation (1.14) becomes

$$-H^2 + \frac{8\pi G}{3}\rho = 0 \tag{1.18}$$

which leads to the definition of the critical density

$$\rho_{cr} = \frac{3H^2}{8\pi G}. \tag{1.19}$$

Equation (1.19) says that, in a flat universe, the total energy density is ρ_{cr}, i.e, in a universe with M components the total energy is

$$\rho_{cr} = \sum_{i}^{M} \rho_i. \tag{1.20}$$

To facilitate comparison between the difference in contributions made by each component to the total energy density, it is useful to define the density parameter, which is a dimensionless quantity

$$\Omega_i = \frac{\rho_i}{\rho_{cr}}, \tag{1.21}$$

and is the fractional contribution of the different components to the energy density of the universe (With the total energy density comprising the sum of all constituents). For a flat universe, $\Omega = 1$. In this dissertation, we denote values of cosmological parameters today with a "0" subscript.

Matter

Matter effectively has zero pressure, and therefore its equation of state parameter w_m, vanishes, so that the matter energy density scales as

$$\rho_m(a) \propto \exp\left\{-3\int^a \frac{da}{a}\right\} = a^{-3}. \tag{1.22}$$

Observations point to the existence of non-baryonic matter, also referred to non-luminous matter since it does not interact in any significant way with radiation. The matter contribution is therefore, $\Omega_m = \Omega_b + \Omega_{dm}$.

Baryons

Current estimates of the baryon density constrain the baryon density to $\sim 2 - 5\%$ of the critical density. BBN, which has already been discussed in section 1.2.2, constrains the baryon density to $\Omega_{b,0}h^2 = 0.020 \pm 0.002$ [51]. Another approach is to look at spectra of distant galaxies, and measuring the amount of light absorption. The amount of light absorbed quantifies the amount of hydrogen the light encounters along the way, the baryon density is then inferred from the estimate of the amount of hydrogen. This approach roughly estimates $\Omega_{b,0}h^2 \simeq 0.020$ [29]. One can also compute the baryon content of the Universe from the anisotropies of the CMB radiation. This approach puts fairly stringent limits on the baryon content to about $\Omega_{b,0}h^2 = 0.024^{+0.004}_{-0.003}$ [45].

Dark Matter

The matter density of a system may also be measured by studying the gravitational field produced by the matter in that system. In the case of spiral galaxies, one can measure the rotation of a galaxy at different distances from its centre and plot the rotational velocity against the distance, the so-called rotational curve. The gravitational field due to spiral galaxies can then be determined by studying their rotational curves. However, this technique estimates about 80% more matter than that inferred from the spectra of these galaxies, pointing to the existence of non-luminous matter. Furthermore, non-luminous estimates of the luminous/baryonic matter predict the matter density to be $20 - 30\%$. One of these techniques uses a phenomena predicted by general relativity– the trajectory of a photon is affected by the curvature of space-time induced by the presence of a massive object (the "lens")– known as gravitational lensing. Current gravitational lensing measurements of the matter density constrain it to $\Omega_{m,0} = 0.248 \pm 0.019$ [51]. Clusters of galaxies, which are the largest known objects, are likely to be representative of the matter in the universe. Therefore, measurements of the baryon to matter ratio in these objects combined with good estimates of the baryonic matter density will give estimates of the dark matter density. The baryon to matter ratio in these objects is roughly 20%. One could also infer the matter density by looking at CMB anisotropies, which constraints the matter density to $\Omega_{m,0} h^2 = 0.1326 \pm 0.00063$ [45]. These independent methods provide compelling evidence that the baryon density is of order of 5% of the critical density, while the total matter density is about five times larger, providing clear evidence for non-baryonic matter. However, dark matter has not been detected directly and all the current evidence is based on its gravitational effects. Currently the most viable candidate for dark matter is known as *cold dark matter* (CDM), which is mostly composed of non-relativistic particles, although, theory also allows for dark matter composed of relativistic particles; hot dark matter (HDM). However, relativistic particles cannot clump together easily, and therefore could not have stimulated the formation of small (on cosmological scales) structures like galaxies and clusters of galaxies. Therefore, dark matter particles are predicted to move slowly to allow them to clump to form the dark matter halos that give the structure of the universe. As a candidate for the CDM particle, the particle physics inspired *weakly interacting particle* (WIMP) was proposed. WIMPs are postulated to interact mainly through the *weak force* and gravity, but not through the *electromagnetic force*, making them the prime candidates for DM particles.

Dark Energy

With matter (baryonic and non-baryonic) making up $\sim 27\%$ of the critical density and indications of spatial flatness, there is clearly a shortfall in the energy density budget. This points to another component in the universe that makes up about two-thirds of the critical density. Furthermore, in 1998, two independent groups (Riess et al. 1998 [30], Perlmutter et al. 1999 [31]) observed a group of SNIa standard candles to be fainter than expected in a matter dominated universe. The manner in which the brightness of standard candles evolves with redshift provides information about the evolution of the universe at late times. Their results are indicative of an

accelerated expansion rate. Since all known matter is attractive, a component with a negative pressure is therefore believed to be driving the accelerated expansion rate. This component is believed to be the cosmological constant which was first introduced by Einstein in order avoid the non-static universe predicted by his theory of General Relativity. The pressure of this component is given by

$$p_\Lambda = -\rho_\Lambda. \tag{1.23}$$

Λ has been interpreted as *vacuum energy*; in quantum physics one possible origin is a type of 'zero-point energy', which remains even in the absence of matter. The density of the cosmological constant, ρ_Λ, is constant throughout the evolution of the universe, i.e., $\Lambda(t) = $ constant. This component has been shown to give rise to the accelerated expansion phase detected by SNIa observations.
Currently the best estimates for the cosmic budget are the WMAP [45] values: $\Omega_{de,0} = 0.734 \pm 0.029$, $\Omega_{dm,0} = 0.222 \pm 0.026$, $\Omega_{b,0} = 0.0449 \pm 0.0028$.

1.4 Quartessence an Alternative to ΛCDM

The ΛCDM model accounts for a wide range of observations, but encounters two theoretical issues. Firstly, according to the standard model of particle physics, Λ must have tiny energy density ($\sim 10^{-47}$ GeV ^{4}). This requirement for a fine-tuned value of Λ, is called the *fine-tuning problem*. The second problems arises when the ΛCDM model is extrapolated back in time to the very early Universe. The dark energy density decreases at a different rate from the matter density, and their ratio shrinks by many orders of magnitude as we extrapolate back in time. Now, the ΛCDM model predicts the ratio was set initially just right so that today, some fourteen billion years later, the ratio is of order unity. It is a remarkable coincidence that somehow we exist in this small (on cosmological scales) epoch when $\Omega_\Lambda/\Omega_m \sim 1$. This is known as the *coincidence problem*. To address the fine tuning and coincidence problems many other models have been proposed, most of which propose a dynamic dark energy. Dynamical dark energy models have a time varying dark energy component, $\Lambda(t)$. Among these, quintessence [7, 8], holographic dark energy [10], quintom [9] and phantom [11] are the most famous. These models attempt to address the fine-tuning problem that arises from the ΛCDM model, and provide a satisfactory fit to observations. However like the ΛCDM model, these models treat dark matter and dark energy as separate entities. However, since there has been no direct detection of either dark matter or dark energy, a scenario where dark dark matter and dark energy are manifestations of the same cosmic fluid has been sought. Such a scenario is called Quartessence or unified dark mater, dark energy (UDME). The *Chaplygin gas* [19, 39], which is a fluid with an exotic equation of state, provides an interesting quartessence scenario. The redshift dependence of this gas is such that at high redshifts (early times), it behaves like matter and low redshift (late times) it behaves like dark energy. However, to successfully model the universe, a sufficient fraction of this fluid has to condense into a gravitationally bound condensate in order to account for structure in the universe. In this dissertation we will study a version of the Chaplygin gas, known

as the variable Chaplygin gas, in light of the CMB observations. Other variations of the Chaplygin gas exist, namely, the Generalised Chaplygin gas [39] and the Modified Chaplygin gas [14]. However, unlike the standard Chaplygin gas, these variations do not have an equivalent brane interpretation [12].

1.5   About This Thesis

In Chapter 2, we describe the growth of the primordial density perturbations. We start with a Newtonian formalism for the growth of a spherically symmetric over-density and then move on to formulate a fully General Relativistic model for a spherically symmetric space-time. We then apply this model to a single fluid model. In Chapter 3, we study how the observed CMB and matter power spectra can be used to test the validity of cosmological models. In Chapter 4, we introduce the idea of quartessence, in particular the Chaplygin gas. We also describe the evolution of the inhomogeneous variable Chaplygin gas. In chapter 5, we first calculate the fraction of VCG that collapses into a gravitationally bound condensate. We then move on to formulate our VCG cosmology. We also describe the FORTRAN 90 code used to do the calculations. In Chapter 6 we discuss the the effects of the VCG on the CMB spectrum and finally in chapter 7 we make our concluding remarks.

Chapter 2

Cosmological Perturbations

The cosmological principle holds on cosmological scales. On smaller scales however, the universe contains density fluctuations ranging from planets to large super clusters and voids. On smaller scales homogeneity and isotropy are clearly violated. This violation of the cosmological principle may be explained by supposing that, in its infancy, the primordial density fluctuations were very close to smooth, with tiny density fluctuations. These tiny density fluctuations have grown by gravitational instability to bring about the complex structure we observe today. As for the origin of the tiny density fluctuations, the widely accepted hypothesis assumes they are quantum fluctuations amplified by a brief period of exponential expansion, known as *inflation*. In this section we study the evolution of the primordial density field. The material in this chapter is based on references [1, 2].

2.1 Formation of Structure

In this section we describe growth of structure. We first describe a linear approach using Newtonian theory, and then we describe a General Relativistic approach to gravitational collapse.

2.1.1 Gravitational Instability

Consider some component of the universe with energy density $\rho(\mathbf{r}, t)$, which depends on position and time. The spatially averaged energy density, at a given time, averaged over some volume V; which is much larger than the largest structure in the universe, is

$$\overline{\rho} = \frac{1}{V} \int_V \rho(\mathbf{r}, t) d^3\mathbf{r}. \tag{2.1}$$

The density contrast is defined as

$$\delta(\mathbf{r}, t) = \frac{\rho(\mathbf{r}, t) - \overline{\rho}(\mathbf{r}, t)}{\overline{\rho}(\mathbf{r}, t)}. \tag{2.2}$$

In overdense regions, $\delta > 0$, and $\delta < 0$ in underdense regions. The density contrast is a minimum, $\delta = -1$, when $\rho = 0$, and there is no definite upper limit on δ. The

study of the growth of structure requires knowing how small density perturbations $\delta \ll 1$, grow in amplitude under the influence of gravity. Before we continue it is useful to define the Jeans Length in a context of a expanding universe. Consider a spherical overdensity with radius R. In the absence of pressure, the time scale for collapse is

$$t_{dyn} \sim (G\overline{\rho})^{-1/2}. \tag{2.3}$$

In the presence of pressure, collapse will be countered by steepening of the pressure gradient within the perturbation. The steepening, however, is not instantaneous, since any changes in pressure travel at the local (of the perturbation) sound speed, c_s. Thus the time it takes for the pressure to build up is

$$t_{pre} \sim \frac{R}{c_s} \,. \tag{2.4}$$

Hydrostatic equilibrium requires the pressure gradient to build up before the overdense region collapses, i.e., the time it takes for the pressure to build up must be less than the collapse time scale. Considering equations (2.3) and (2.4), one can conclude that for a density perturbation to be stabilised by pressure against collapse, it must be smaller by some characteristic size λ_J, the so-called Jeans Length

$$\lambda_J \sim c_s t_{dyn} \sim (G\overline{\rho})^{-1/2} \,, \tag{2.5}$$

including all the factors of π, the Jeans Length is

$$\lambda_J = 2\pi c_s t_{dyn} \,. \tag{2.6}$$

Overdense regions of scales larger than the Jeans length will collapse under their own gravity, while regions smaller than the Jeans length oscillate in density. Now consider a flat expanding universe with average density $\overline{\rho}$, and with fluctuations of amplitude $|\delta| \ll 1$. The characteristic time for expansion in such a universe is the Hubble time,

$$H^{-1} = \left(\frac{3c^2}{8\pi G\overline{\rho}} \right)^{1/2} \,, \tag{2.7}$$

which, together with equation (2.3), leads to

$$H^{-1} = \left(\frac{3}{2} \right)^{1/2} t_{dyn} \,. \tag{2.8}$$

The Jeans length in an expanding universe therefore becomes

$$\lambda_J = 2\pi c_s t_{dyn} = 2\pi \left(\frac{3}{2} \right)^{1/2} \frac{c_s}{H} \,. \tag{2.9}$$

2.1.2   A Newtonian Approach

A Newtonian approach is sufficient to study the growth of small perturbations in a flat expanding universe. Consider a matter filled universe, with density $\rho(\mathbf{r}, t)$.

Within a spherical slightly ($\delta \ll 1$) overdense region of radius R, the density within the sphere is

$$\rho(t) = \overline{\rho}(t)[1 + \delta(t)] .$$

(2.10)

The total gravitational acceleration at the surface of the sphere is

$$\ddot{R} = -\frac{GM}{R^2} = -\frac{G}{R}\frac{4\pi}{3}\rho R^3 = -\frac{4\pi}{3}GR\left(\overline{\rho} + \delta\overline{\rho}\right) .$$

(2.11)

The equation of motion for a point at surface of the sphere is

$$\frac{\ddot{R}}{R} = -\frac{4\pi}{3}G(\overline{\rho} + \delta\overline{\rho}) .$$

(2.12)

Mass conservation requires the mass inside the sphere

$$M = \frac{4\pi}{3}\overline{\rho}(t)[1 + \delta(t)]R^3(t) ,$$

(2.13)

to remain constant as the universe expands, leading to

$$R(t) \propto \overline{\rho}(t)^{-1/3}[1 + \delta(t)]^{-1/3} .$$

(2.14)

Since this universe is matter-dominated, $\overline{\rho} \propto a^{-3}$, we also have

$$R(t) \propto a(t)[1 + \delta(t)]^{-1/3}.$$

(2.15)

Equation (2.15) implies that if the sphere is slightly overdense, its radius will grow slightly less rapidly than the scale factor. If the sphere is slightly is slightly underdense it will grow slightly more rapidly than the scale factor. The time derivative of (2.15) is

$$\dot{R} \propto \dot{a}[1 + \delta]^{-1/3} - \frac{1}{3}a[1 + \delta]^{-4/3}\dot{\delta} ,$$

(2.16)

and the second time derivative is

$$\ddot{R} \propto \ddot{a}[1 + \delta]^{-1/3} - \frac{2}{3}\dot{a}[1 + \delta]^{-4/3}\delta\left(1 - \frac{2}{3}[1 + \delta]^{-1}\delta\right) - \frac{1}{3}[1 + \delta]^{-4/3}\ddot{\delta} .$$

(2.17)

Considering that $\delta \ll 1$, then dividing by equation (2.15) yields

$$\frac{\ddot{R}}{R} \simeq \frac{\ddot{a}}{a} - \frac{1}{3}\ddot{\delta} - \frac{2}{3}\frac{\dot{a}}{a}\dot{\delta} ,$$

(2.18)

then (2.12) and (2.18) lead to the acceleration equation for a such a slightly perturbed matter-dominated homogeneous, isotropic universe,

$$\frac{\ddot{a}}{a} - \frac{1}{3}\ddot{\delta} - \frac{2}{3}\frac{\dot{a}}{a}\dot{\delta} = -\frac{4\pi}{3}G(\overline{\rho} + \delta\overline{\rho}) ,$$

(2.19)

which, when $\delta = 0$, reduces to the acceleration for a homogeneous, isotropic matter-dominated universe

$$\frac{\ddot{a}}{a} = -\frac{4\pi}{3}G\overline{\rho} .$$

(2.20)

To find an expression that describes how small perturbations grow, equation (2.20) may be subtracted from equation (2.19) leaving only terms linear in δ:

$$\frac{1}{3}\ddot{\delta} + \frac{2}{3}\frac{\dot{a}}{a}\dot{\delta} = \frac{4\pi}{3}G\delta\bar{\rho} \tag{2.21}$$

or, using equation (1.13)

$$\ddot{\delta} + 2H\dot{\delta} = 4\pi G\delta\rho. \tag{2.22}$$

This form of the equation can be applied to a universe with non-negligible pressure, such as the cosmological constant. However in a multi-component universe, δ represents the fluctuations only in the matter density. Equation (2.22) may be written in terms of the matter density parameter,

$$\ddot{\delta} + 2H\dot{\delta} - \frac{3}{2}\Omega_m H^2\delta = 0 \,. \tag{2.23}$$

During epochs when matter does not dominate the universe, δ does not grow rapidly in amplitude. For instance, during the radiation domination era($H = 1/2t$, $\Omega \ll 1$), equation (2.23) becomes

$$\ddot{\delta} + \frac{1}{t}\dot{\delta} \approx 0 \,, \tag{2.24}$$

which has solution

$$\delta(t) \approx B_1 + B_2\ln(t) \,. \tag{2.25}$$

During radiation dominance, the matter perturbations grow at a logarithmic rate. And more recently, during the dark energy (cosmological constant) domination era, equation (2.23) becomes

$$\ddot{\delta} + 2H_\Lambda\dot{\delta} \approx 0 \,, \tag{2.26}$$

with solution

$$\delta(t) \approx C_1 + C_2 e^{-2H_\Lambda t} \,. \tag{2.27}$$

In a Λ-dominated universe, the matter fluctuations asymptotically approach a constant fractional amplitude. When matter-dominates the energy density of the universe, there is a significant growth in the amplitude of the density fluctuations. In this case, $H = 2/3t$, $\Omega_m = 1$:

$$\ddot{\delta} + \frac{4}{3t}\dot{\delta} - \frac{2}{3t^2}\delta = 0 \,, \tag{2.28}$$

One may try a power-law solution of the form $\delta(t) = Dt^n$,

$$n(n-1)Dt^{n-2} + \frac{4}{3t}nDt^{n-1} - \frac{2}{3t^2}Dt^n = 0 \,, \tag{2.29}$$

or

$$n(n-1) + \frac{4}{3}n - \frac{2}{3} = 0 \,. \tag{2.30}$$

This quadratic equation has solution, $n = -1, 2/3$, giving general solution

$$\delta(t) = D_1 t^{2/3} + D_2 t^{-1} \,. \tag{2.31}$$

The initial conditions for $\delta(t)$ can be used to determine, D_1, D_2. The decaying mode $D_2 t^{-1}$ eventually becomes insignificant compared to the growing mode $d_1 t^{2/3}$ as t grows. It is worth remembering that this evolution of the density fluctuations holds as long $\delta \ll 1$. When $\delta \sim 1$, the above approach becomes unreliable to study the evolution of density fluctuations. To study the evolution of $\delta \sim 1$ and $\delta > 1$ computer simulations can be used. In these simulations, when a region reaches an overdensity $\delta \sim 1$, it breaks away from the Hubble flow and collapses. The overdense region oscillates a few times then and attains viral equilibrium as gravitationally bound structure. Baryonic matter evolves to form the stellar part of galaxies, while the dark-matter forms the dark halos within which the stellar components of galaxies are embedded [1].

2.1.3   A Full GR Approach

In this section we describe a spherically symmetric inhomogeneity. We mainly follow the full General Relativistic formalism presented in [12]. The space-time of a spherically symmetric inhomogeneity is described by the metric [12]

$$ds^2 = N(t,r)^2 dt^2 - b(t,r)^2 (dr^2 + r^2 S_\kappa(t,r)d\Omega^2) , \tag{2.32}$$

where N is the local lapse function, b is the local expansion factor and $S_\kappa(t,r)$ describes spatial curvature. In the limit $r \to \infty$, the above metric approaches the FRW metric, i.e., $N(r,t) \to 1$, $S_\kappa \to 1$ and $b(r,t) \to a(t)$. The Hubble parameter in a space-time described by the metric (2.32) is given by [12]

$$H = \frac{1}{N} \left(\frac{b_{,0}}{b} + \frac{1}{3} \frac{S_{\kappa,0}}{S_\kappa} \right) \tag{2.33}$$

and the shear is given by

$$\sigma^2 = \frac{2}{3} \left(\frac{1}{2N} \frac{S_{\kappa,0}}{S_\kappa} \right)^2 . \tag{2.34}$$

Assuming the density contrast to be of fixed Gaussian shape with comoving size R, the energy density evolves as

$$\rho(t,r) = \bar\rho(t)[1 + \delta(t,R) e^{-r^2/(2R^2)}] . \tag{2.35}$$

The density contrast is given by

$$\delta(a) = \frac{\rho(a) - \bar{\rho(a)}}{\bar{\rho(a)}} , \tag{2.36}$$

where background quantities are bared. Since every region is treated as being independent in spherical models, the spatial derivatives of N, ρ, b vanish at the origin. Hence we may expand b and N about the origin as follows

$$\begin{aligned} N(r,t) &= N(t,0) \left[1 + \mathcal{O}(r^2))\right] \tag{2.37} \\ b(r,t) &= b(t,0) \left[1 + \mathcal{O}(r^2))\right] . \tag{2.38} \end{aligned}$$

Now, evaluating Einstein's equation $G^0{}_1 = 0$ leads to [12]

$$2\frac{b_{,1}}{b} + \frac{b_{,1}}{b}\left(\frac{S_{\kappa,0}}{S_\kappa} - 2\frac{b_{,0}}{b}\right) - \frac{N_{,1}}{N}\left(2\frac{b_{,0}}{b} + \frac{S_{\kappa,0}}{S_\kappa}\right) + \frac{S_{\kappa,0}}{S_\kappa}\left(\frac{1}{r} - \frac{1}{2}\frac{S_{\kappa,1}}{S_\kappa}\right) = 0 . \quad (2.39)$$

Recalling that the first three terms vanish at origin, the above equality holds only if $\frac{S_{\kappa,0}}{S_\kappa} = 0$ at the origin. Looking at Equation (2.34) we see that the shear vanishes at the origin.

For a one-component model, the Raychaudhury equation

$$3\dot{H} + 3H^2 + \sigma_{\mu\nu}\sigma^{\mu\nu} + u^\mu u^\nu R_{\mu\nu} = \dot{u}^\mu{}_{;\mu} . \quad (2.40)$$

combines with Einsteins equations (1.1) to give [12]

$$3\dot{H} + 3H^2 + \sigma^2 + 4\pi G(\rho + 3p) = \left(\frac{c_s^2 h^{\mu\nu}\rho_{,\nu}}{p + \rho}\right)_{;\mu} . \quad (2.41)$$

Evaluating this equation at the origin we get

$$\frac{1}{N(t,0)}\frac{dH(t,0)}{dt} + H(t,0)^2 + \frac{4\pi G}{3}(\rho(t) + 3p(t)) = \frac{c_s^2(\rho(t) - \bar{\rho}(t))}{b(t,0)^2 R^2(p(t) + \rho(t))} . \quad (2.42)$$

From now on we denote the inhomogeneity quantities evaluated at the origin as, $H(t,0) = H$, $b(t,0) = 0$, $N(t,0) = N$. Therefore we rewrite Equation (2.42) as

$$\frac{1}{N}\frac{dH}{dt} + H^2 + \frac{4\pi G}{3}(\rho + 3p) = \frac{c_s^2\,\delta\bar{\rho}}{b^2 R^2(p + \rho)} . \quad (2.43)$$

The evolution of $\rho(t)$ may described the continuity equation

$$\frac{d\rho}{dt} + 3H(\rho + p) = 0. \quad (2.44)$$

Then with an equation of state $p = p(\rho)$, the growth of a spherically symmetric inhomogeneity of a one-component fluid is described by Equations (2.43) and (2.44). Looking at Equation (2.33), the Hubble parameter evaluated at the origin is

$$H = \frac{1}{b}\frac{db}{dt} . \quad (2.45)$$

2.1.4 Statistics of Collapsed Objects: The Press-Schechter Theory

Up to this point, we have discussed a theory that describes the evolution of the density fluctuations set up during inflation. However, thus far, the theory cannot predict the fraction of matter that has collapsed into non-linear structure. For instance, one may predict the matter distribution in the universe but cannot predict the number density of galaxies. The Press-Schechter formalism is the basis for much of the work that studies the statistics of collapsed objects [16]. The idea is that for a given spherical volume of radius R, if the density contrast inside exceeds a certain critical value δ_c, then the mass in this volume will collapse and form a dark matter halo of mass $M = (4\pi/3)R^3\rho$. With a Gaussian random field,

$$\mathcal{P}(\delta, R)d\delta = \frac{d\delta}{\sqrt{2\pi\sigma^2(R)}}\exp\left(\frac{\delta^2}{2\sigma^2(R)}\right) , \qquad (2.46)$$

the probability of finding collapsed objects of mass greater than M can be obtained by the integral

$$F(R) = 2\int_{\delta_c} \mathcal{P}(\delta, R)d\delta \;=\; 2\int_{\delta_c} \frac{d\delta}{\sqrt{2\pi}\sigma(R)}\exp\left(-\frac{\delta^2}{2\sigma^2(R)}\right) \qquad (2.47)$$

$$=\; \mathrm{erfc}\left(\frac{\delta_c}{\sqrt{2}\sigma(R)}\right) , \qquad (2.48)$$

where $\sigma(R)$ is the variance in matter fluctuations at a scale R, defined by

$$\sigma(R) = \int_0 \frac{dk}{k}\exp\left(-k^2 R^2\right)\Delta^2(k) , \qquad (2.49)$$

and where $\Delta(k)$ is defined by equation (3.14). The normalisation factor of 2, in equation (2.47) is required to account for underdense regions that can exist within overdense regions, this effect is known as the *cloud-in-cloud* problem, which is not predicted by the original theory. Nevertheless, with the inclusion of this normalisation factor, Numerical simulations have shown that this method to work extremely well [17] and [18]. The value of δ_c, is predicted by linear theory to be $\delta_c = 1.686$, in a flat dark matter-dominated universe.

In section 5.1.1 we will use this formalism to estimate the fraction of the variable chaplygin gas that collapses under the influence of gravity to form structure.

Chapter 3

Cosmological Observations

In order to evaluate whether a cosmological model is viable, we require a means of comparing its predictions with observational data. As described in section 1.2.3, the CMB is a rich source of information about the state of perturbations in the universe at the last scattering surface. Another observation which is just as important as the CMB is the observed distribution of galaxies. Galaxies are organised in clusters of galaxies which in turn form super-clusters that are separated by large voids. This structure of the universe is often referred to as the *cosmic web*. Figure 3.1 shows the distribution of galaxies from the Sloan Digital Sky Survey (SDSS) main galaxy redshift sample. The SDSS is an imaging and redshift survey that uses a 2.5 meter wide-angle optical telescope. The SDSS imaging results cover over 35% of the full sky with photometric observations of around 500 million objects and spectra for more than a million objects. The main galaxy sample of this survey is at redshift $z \sim 0.1$ [44].
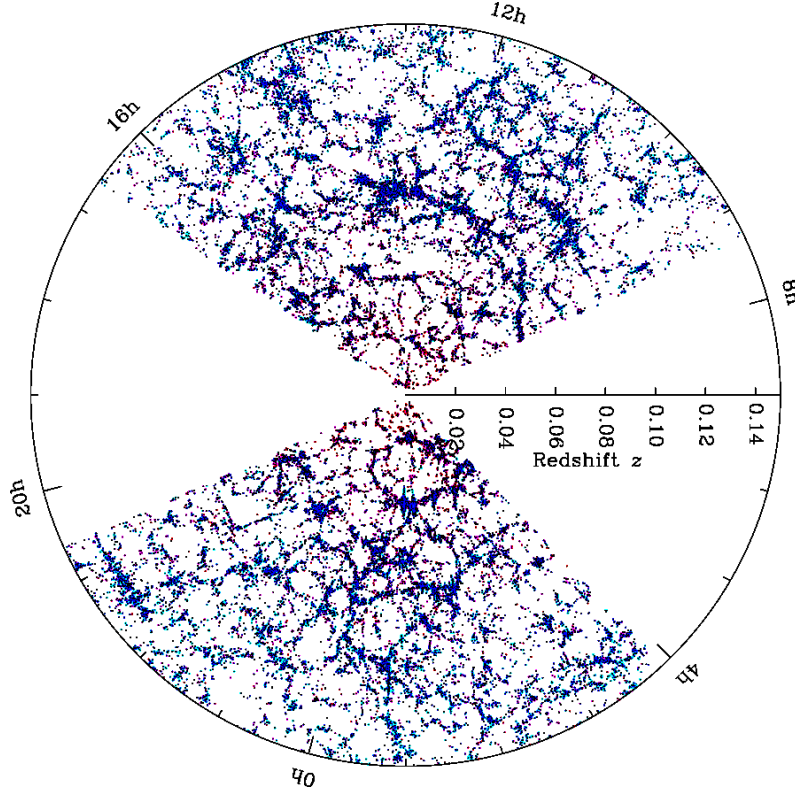
Figure 3.1: Large scale structure in the northern equatorial slice of the SDSS main galaxy redshift sample [42]. The slice is 2.5 degrees thick.

This observation is important since this structure must be linked to the initial density fluctuations set up during inflation. Therefore a viable cosmology has to account for, and have the primordial density fluctuations that have evolved to form the large scale structure we observe on large scales today. In this chapter we describe how the theory that describes the evolution of the primordial density fluctuations may be compared with observational data. The subsequent description of the matter and temperature fluctuations will only highlight the important results, assumptions and definitions.

3.1 The Power Spectrum

The previous chapter described the evolution of the primordial density field. To compare theory with observations, i.e., to make quantitative tests of cosmological models, it is necessary to know how to characterise the CMB fluctuations and large scale structure distribution. Cosmological theories are expected to predict the statistical properties of the Universe and not, for example, the exact positions of each overdensity in the dark matter distribution. Therefore, power spectra are very important tools in cosmology, as they can give quantitative information about the variations of a field on different scales. In this section we will study the CMB (temperature fluctuations) and matter power (large scale structure) spectra. We mainly follow the formalism in given in [1, 2].

3.1.1 The Matter Power Spectrum

In the case of the large scale structure observations it is useful to take the Fourier transform of the galaxy distribution map in Figure 3.1. The advantage of working in Fourier space is that its easier to distinguish between large and small scales. Working in Fourier space, the most important statistic about the observed large scale structure is the variance in the distribution, known as the matter power spectrum $P(k)$: Consider the Fourier transform of the density fluctuation $\delta(\mathbf{r})$,

$$\delta(\mathbf{k}) = \int \delta(\mathbf{r})e^{-i\mathbf{k}r}d^3r. \tag{3.1}$$

The power spectrum is then defined as

$$\langle\delta(\mathbf{k})\delta(\mathbf{k}')\rangle = (2\pi)^3 P(k)\delta^3(\mathbf{k}-\mathbf{k}'), \tag{3.2}$$

where δ^3 is the Dirac delta function which constrains $\mathbf{k} = \mathbf{k}'$.

The construction of the matter power spectrum requires a solution to the evolution of each Fourier mode $\delta(k,\eta)$ and the initial power spectrum generated by inflation. Performing the Fourier transform effectively means breaking up the function $\delta(\mathbf{r})$ into an infinite number of sine waves, each with comoving wavenumber $\mathbf{k}$, and comoving wavelength $\lambda = 2\pi/k$. In conformal time, the density perturbations can be written as

$$\delta(\mathbf{k},\eta) \propto k^2 T(k)\phi(\mathbf{k},\eta_i)D(\eta) \tag{3.3}$$

where $\phi(\mathbf{k},\eta_i)$ is the primordial gravitational potential at some initial time η_i and $T(k)$ is known as the *transfer function*. The transfer function which describes the evolution of the perturbations is a function of scale, while the growth factor $D(\eta)$ describes the scale independent independent growth at later times. Equation (3.3) together with definition of the power spectrum, equation (3.2), yield

$$P(k) \propto k^4 T^2(k)\langle\phi(\mathbf{k},\eta_i)^2\rangle D^2(\eta). \tag{3.4}$$

We relate the potential during this late epoch to the primordial potential, this is achieved through

$$\phi(\mathbf{k},\eta) = \frac{9}{10}\phi(\mathbf{k},a_i)T(k)\frac{D_1(a)}{a} \tag{3.5}$$

where the transfer function is defined as

$$T(k) = \frac{\phi(k,a_{\text{late}})}{\phi_{\text{large-scale}}}. \tag{3.6}$$

This definition is of the transfer function is such that its value is unity on large scales. This is achieved by neglecting the decline in wavelength perturbations as they enter matter-radiation equality. By defining the ratio of the potential to its value at late epochs as

$$\frac{\phi(a)}{\phi(a_{\text{late}})} = \frac{D_1(a)}{a}, \tag{3.7}$$

D_1 becomes the growth of matter perturbations at late times.

Poisson's equation may be used to relate the matter perturbations and the potential:

$$\phi(\mathbf{k}, a) = \frac{4\pi G \rho_m a^2 \delta(\mathbf{k}, a)}{k^2}, \tag{3.8}$$

and recalling how matter evolves with scale factor, $\rho_m = \Omega_{m,0}\rho_{cr,0}/a^3$ and the definition $\rho_{cr,0} = \frac{3H_0^2}{8\pi G}$, leads to

$$\delta(\mathbf{k}, a) = \frac{2}{3} \frac{k^2 \phi(\mathbf{k}, a) a}{\Omega_m H_0^2}, \tag{3.9}$$

which may be combined with equation (3.5), to give an expression that relates the overdensity today to the primordial potential:

$$\delta(\mathbf{k}, a) = \frac{3}{5} \frac{k^2}{\Omega_m H_0^2} \phi(\mathbf{k}, a_i) T(k) D_1(a). \tag{3.10}$$

This equation is independent of how the initial potential $\phi(\mathbf{k}, a_i)$ was generated, but in the context of inflation, $\phi(\mathbf{k}, a_i)$ is drawn from a Gaussian distribution with mean variance

$$P_\phi = \frac{50\pi}{9k^3} \left(\frac{k}{H_0}\right)^{n-1} \delta_H^2 \left(\frac{\Omega_m}{D_1(a=1)}\right)^2, \tag{3.11}$$

so the power spectrum at late times is

$$P(k, a) = 2\pi^2 \delta_H^2 \frac{k^n}{H_0^{n+3}} T^2(k) \left(\frac{D_1(a)}{D_1(a=1)}\right)^2, \tag{3.12}$$

where δ_H^2 is the perturbation amplitude at horizon crossing. The power spectrum has dimensions of (length)^3, but to expresses it as a dimensionless quantity, one may associate $d^3k P(k)/(2\pi)^3$ with the excess power in a bin of width k centred at k. Integrating over all orientations of k gives

$$d^3k P(k)/(2\pi)^3 = \frac{dk}{k} \Delta^2(k), \tag{3.13}$$

where

$$\Delta^2(k) = \frac{k^3 P(k)}{2\pi^2}. \tag{3.14}$$

Figure 3.2 shows the concordance model matter power spectrum. On large scales the power increases as function of increasing k, then beyond some k_{cr} the power decreases as function of k on small scales. To explain this turn-over on small scales, consider that small scales enter the horizon well before matter-radiation equality, i.e., during the radiation epoch, when the potential decays and therefore the transfer function is much smaller than unity. Small scale modes are therefore suppressed from the time they enter the horizon up until the epoch when matter dominates. Thus the power spectrum is a decreasing function of k on small scales.
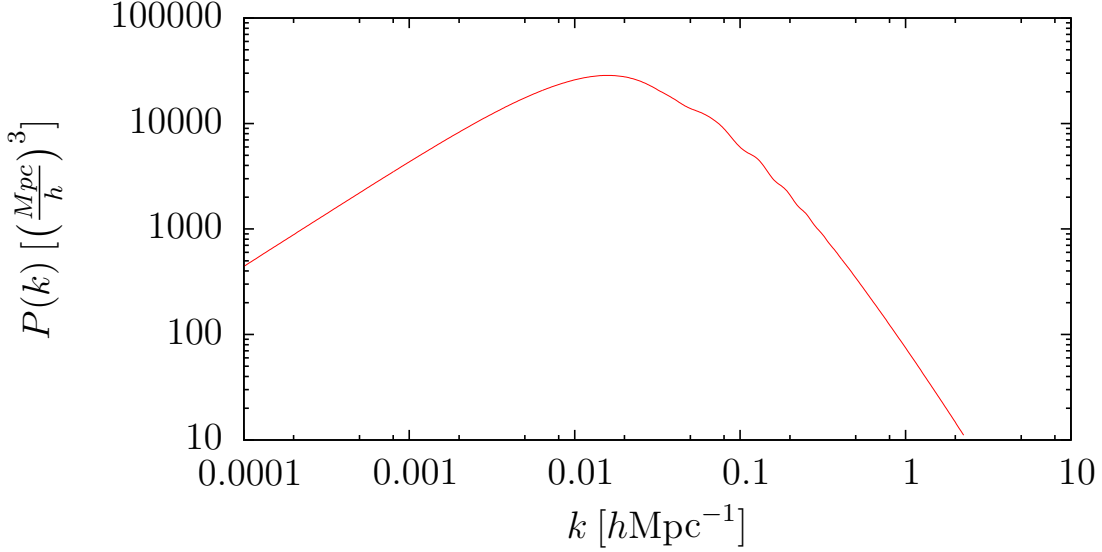
Figure 3.2: Shows the matter power spectrum for the ΛCDM constructed from the WMAP-9 cosmological parameters [45]. This plot was generated using CAMB [49].

3.1.2 The CMB Anisotropy Spectrum

The CMB is observed today as a isotropic radiation field that is very smooth on large scales. However, correcting our relative motion to the CMB rest frame reveals tiny anisotropies in the CMB temperature, of order $\Delta T/T \sim 10^-5$. To first order, these fractional anisotropies only depend on the direction $\hat{n}$ of the observer. The CMB may be taken to be a 2D-field on the surface of a sphere; one may expand the CMB temperature distribution in spherical harmonics. Therefore the two-point function is a function of multipole moment ℓ, instead of the wavenumber k:

$$\frac{\Delta T(\hat{n})}{T} = \sum_{\ell=2} \sum_{m=-\ell}^{\ell} a_{\ell m} Y_{\ell m}(\hat{n}), \tag{3.15}$$

where the $a_{\ell m}$ are the multipole co-efficients and the $Y_{\ell m}$ are the spherical harmonics. Each ℓ corresponds to an angular scale given by $\theta \approx 180°/\ell$. Now assuming that the temperature perturbations follow a Gaussian distribution and are statistically isotropic, the power $\mathcal{C}_\ell$ on angular scales ℓ, may be defined by

$$\langle a_{\ell'm'} a_{lm} \rangle = \mathcal{C}_\ell \, \delta_{\ell'\ell} \, \delta_{m'm}. \tag{3.16}$$

The distribution is assumed to Gaussian to ensure that the power spectrum $\mathcal{C}_\ell$ contains all the information, making it the only quantity required to characterise the temperature field. The Kronecker delta's, $\delta_{i'i}$, ensure that the power distribution through the multipoles is a function of angular scale. The observed angular power spectrum is given by

$$\mathcal{C}_\ell = \frac{1}{2\ell+1} \sum_{m=-\ell}^{\ell} |a_{\ell m}|^2, \tag{3.17}$$

where $\mathcal{C}_\ell$ is assumed to contain all the statistical information characterising the temperature field, defined by (3.16).

Relating the CMB anisotropies to the density fluctuation, which can be predicted by cosmological models, is the key to extracting the information that was encoded within the CMB temperature field by the cosmic fluid at the last scattering surface. Assume that the temperature field is given by

$$T(\mathbf{r}, \hat{n}, \eta) = T(\eta)(1 + \Theta(\mathbf{r}, \hat{n}, \eta)), \tag{3.18}$$

where Θ is characteristic of the photon perturbation distribution function. The field Θ may be expanded in terms of spherical harmonics [2]:

$$\Theta(\mathbf{r}, \hat{n}, \eta) = \sum_{\ell=1} \sum_{m=-1}^{\ell} a_{\ell m}(\mathbf{r}, \eta) Y_{\ell m}(\hat{n}). \tag{3.19}$$

Then using the spherical harmonics othornomality property [2],

$$\int d\Omega Y_{\ell m}(\hat{n}) Y_{\ell m'}^*(\hat{n}) = \delta_{\ell \ell'} \delta_{mm'}$$

, and inverting equation (3.19) by multiplying both sides by $Y_{\ell m}^*(\hat{n})$ and integrating to obtain

$$a_{\ell m}(\mathbf{r}, \eta) = \int \frac{d^3 k}{(2\pi)^3} e^{i\mathbf{k}\cdot\mathbf{r}} \int d\Omega Y_{\ell m}^*(\hat{n}) \Theta(\mathbf{k}, \hat{n}, \eta), \tag{3.20}$$

we may write the angular power spectrum, as defined by equation (3.16), as

$$\mathcal{C}_\ell = \int \frac{d^3 k}{(2\pi)^2} \int d\Omega Y_{\ell m}(\hat{n}) \Theta(k, \hat{k}\cdot\hat{n}) \int d\Omega Y_{\ell m}(\hat{n}) \Theta^*(k, \hat{k}\cdot\hat{n}) \tag{3.21}$$

where $\Theta(\mathbf{k}, \hat{n}, \eta)$ is the Fourier transform of $\Theta(\mathbf{r}, \hat{n}, \eta)$. Now to obtain an expression for $\mathcal{C}_\ell$, one needs $\langle \Theta(\mathbf{k}, \hat{n}, \eta) \Theta^*(\mathbf{k}, \hat{n}, \eta) \rangle$. This expectation value depends on two separate phenomena: (i) the initial amplitude and the phase of the perturbation is chosen during inflation from a Gaussian distribution and (ii) the evolution of the initial perturbation that turns into anisotropies, i.e., produces the $\hat{n}$ dependence. To simplify, one may write the photon distribution as $\delta \times (\Theta/\delta)$, where the dark matter overdensity does not depend on any directional vector. (Θ/δ) does not depend on the initial amplitude, so it can be removed from the averaging over the distribution

$$\langle \Theta(\mathbf{k}, \hat{n}, \eta) \Theta^*(\mathbf{k}, \hat{n}, \eta) \rangle = \langle \delta(\mathbf{k}) \delta^*(\mathbf{k}) \rangle \left(\frac{\Theta(\mathbf{k}, \hat{n}, \eta)}{\delta(\mathbf{k})} \right) \left(\frac{\Theta^*(\mathbf{k}, \hat{n}, \eta)}{\delta^*(\mathbf{k})} \right) \tag{3.22}$$

Then, recall the definition of the matter power spectrum ((3.2)). The ratio δ/Θ depends only on the magnitude of $\mathbf{k}$ and the dot product $\hat{k}\cdot\hat{n}$: two modes with the same $\mathbf{k}$ and $\hat{k}\cdot\hat{n}$ evolve identically regardless of their initial conditions or phase (from now on, the dependence on η may be taken to be implicit). Thus,

$$\langle \Theta(\mathbf{k}, \hat{n}) \Theta^*(\mathbf{k}, \hat{n}) \rangle = (2\pi)^3 P(k) \delta^3(\mathbf{k} - \mathbf{k}) \left(\frac{\Theta(k, \hat{k}\cdot\hat{n})}{\delta(k)} \right) \left(\frac{\Theta(k, \hat{k}\cdot\hat{n})}{\delta^*(\mathbf{k})} \right). \tag{3.23}$$

Then combining equation (3.21) with equation (3.23), the angular power spectrum may be related to the density perturbations through

$$\mathcal{C}_\ell = \int \frac{d^3k}{(2\pi)^2} \int d\Omega Y_{\ell m}(\hat{n}) \frac{\Theta(k, \hat{k} \cdot \hat{n})}{\delta(k)} \int d\Omega \, Y_{\ell m}(\hat{n}) \frac{\Theta^*(k, \hat{k} \cdot \hat{n})}{\delta(k^*)}. \qquad (3.24)$$

It can be further shown that the angular power spectrum (CMB anisotropies) is related to the matter power spectrum (density fluctuations) through

$$\mathcal{C}_\ell = \frac{2}{\pi} \int_0 \; dk \, k^2 P(k) \left| \frac{\Theta_\ell(k)}{\delta(k)} \right|^2. \qquad (3.25)$$

Generation of CMB Anisotropies

We now present a qualitative description of the mechanism that generates the CMB anisotropies; then we move on to study features of the CMB spectrum.

CMB Anisotropies may be grouped into two categories; primary anisotropies are the anisotropies generated at the last scattering surface and secondary anisotropies are generated along the CMB photon's path to us. The fluctuations δ_γ already present in the photon density at the surface of last scattering create anisotropies in the CMB. CMB anisotropies are also generated when the CMB photons are gravitationally redshifted or blueshifted by time evolving gravitational potentials. Fluctuations in the matter density will give rise to 'local' potential wells (minima) and hills (maxima). Photons lose energy in climbing out of the potential well and are consequently redshifted, while they gain energy when they roll off a potential hill, and are consequently blueshifted. Therefore depending on whether a CMB photon was in potential well or a potential hill at the time of last scattering, its temperature will either be subtly higher or lower. This mechanism of creating temperature fluctuations by variations in the gravitational potential is known as the *Sachs-Wolfe effect* [43]. The potential wells and hills present at decoupling do not evolve with time as long the universe is matter dominated, and therefore do not generate more anisotropies. However, at a redshift of about $z = 0.6$ the energy density becomes dominated by dark energy. Then the potential wells and hills are no longer static, these time evolving gravitational potentials generate more temperature fluctuations in the CMB photons. This effect is known as the *integrated Sachs-Wolfe effect* (ISW) [43]. Furthermore, bulk velocities of the baryon-photon fluid relative to an observer causes a Doppler shift which also contributes to the CMB anisotropies. To summarise:

$$\frac{\Delta T}{T}(\hat{n}) = \frac{1}{4}\delta_\gamma + \phi(\hat{n}) + \frac{1}{4}\delta_\gamma - \mathbf{n} \cdot \mathbf{u} + \int_{lss}^{\eta_0} \frac{d\phi}{d\eta} \qquad (3.26)$$

where the first term is due to gravitational redshifting by the gravitational potential wells and hills, the Sachs-Wolfe effect. The second term arises from the already existing photon density fluctuations, which are characterised by the Stephen-Boltzmann law $\rho_\gamma = \sigma T^4$ (where σ is the Stephen Boltzmann constant). The third term is due to the relative motion of the baryon-photon fluid with respect to us and

the fourth term is due to the ISW effect.

Figure 3.3 shows the CMB anisotropy spectrum, computed using the concordance model with the WMAP-7 best fit cosmological parameters:ΛCDM model; $H_0 = 71.0$, $\Omega_c = 0.222$, $\Omega_b, = 0.0449$.
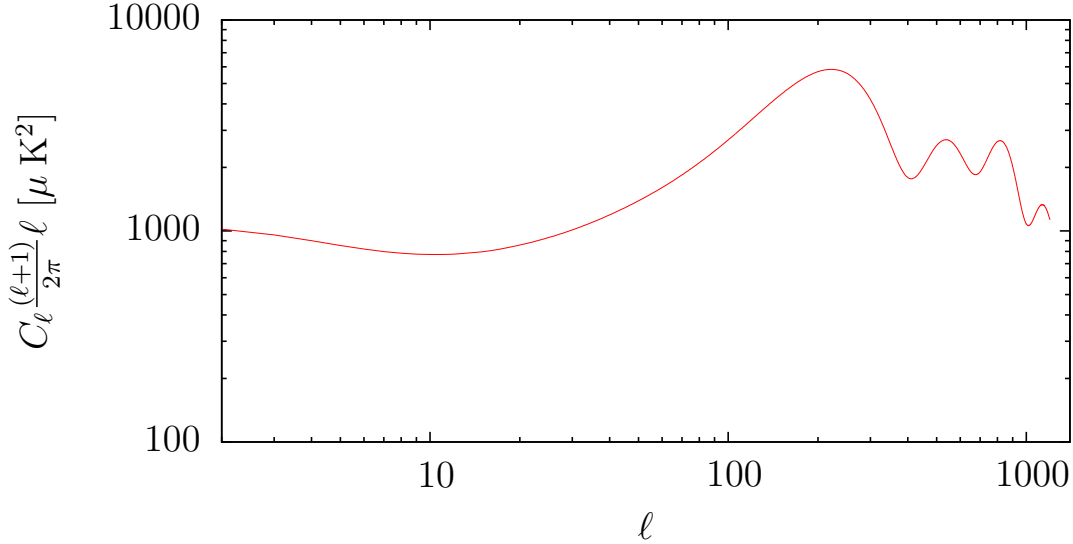

Figure 3.3: Shows ΛCDM CMB Anisotropy spectrum constructed from the WMAP-9 cosmological parameters[45]. This plot was generated using CAMB [49].

During the period just before the CMB photons were liberated from the baryons cosmic expansion had cooled the CMB photons to a temperature of about $T \sim 3000k$. During this epoch, the electrons couple the baryons to the photons by Compton scattering and electromagnetic interactions, resulting a singe baryon-photon fluid. Gravity attracts and compresses the fluid into the potential wells and hills. Photon pressure counters the compression and sets up acoustic oscillations in the fluid. These acoustic oscillations are frozen into the distribution of photons at recombination. During the radiation domination epoch, the pressure gradients due to the gravitational potentials from matter can be neglected. However, once the gradients have turned infall into acoustic oscillations and the potentials decay, leading to lower amplitudes in the subsequent oscillations.

At the same time the universe continues to cool adiabatically to a point where the photons and baryons decouple. These photons are the CMB photons we detect today, which have free streamed from the point of decoupling. Figure 3.3 shows the CMB anisotropy spectrum, this spectrum is computed using the *code for anisotropies in the CMB* (CAMB) [49].

In order to study the CMB anisotropy features, we consider a fiducial ΛCDM cosmology constructed from the Wilkinson Microwave Anisotropy Probe (WMAP)-9yr best fit cosmological parameters [45]. The WMAP is a satellite which measures CMB radiation across the full sky. WMAP measurements play a key role constraining cosmological models, and are well fitted by the current concordance model. In the context of a flat universe, we wish to study the effects of varying some of the ΛCDM cosmological parameters in turn.

- Increasing $\Omega_{b,0}$ increases the amplitudes of the odd peaks over the even peaks, while decreasing $\Omega_{b,0}$ decreases the amplitudes of the even peaks over the odd ones. This is because baryons drag the baryon-photon fluid deeper into the potential wells. This results in the compressional (odd) peaks being enhanced by the baryons and the rarefaction (even) peaks being suppressed [28].

- Decreasing $\Omega_{c,0}$ boosts the amplitudes of all the peaks. This predominately affects the higher ℓ, which correspond to the matter-radiation equality epoch, essentially because decreasing $\Omega_{c,0}$ reduces the matter-radiation ratio.

- Varying $\Omega_{\Lambda,0}$ in a flat universe is at the cost of varying $\Omega_{c,0}$ and visa-versa, so this case is included in the second point.

In ΛCDM, $w_\Lambda(a) = -1$. However, since the goal of this thesis is study the effects of a time varying dark energy model we also wish to study the effect of a time varying w on the CMB. Therefore we consider a simple dynamical dark energy model described by the linear relation [53]

$$w_{de}(a) = \alpha + (1-a)\beta \qquad (3.27)$$

where the constants α and β are chosen such that $-1 \leq w_{de}(a) \leq 0$. We then compare the CMB spectra from this model to that obtained from ΛCDM for the same H_0, $\Omega_{b,0}$ and $\Omega_{c,0}$. Figure 3.4 shows CMB spectra obtained from the dark energy model defined by Equation (3.27) for $\{\alpha, \beta\} = \{-1, 0.9\}, \{-1, 0.5\}$ (green,blue) and the red curve is the ΛCDM spectrum. These plots are for the same cosmological parameters except that they have different equation of state parameters. For the model with $\beta = 0.5$, the equation of state parameter deviates from -1 at an earlier time, i.e., the model tends towards ΛCDM later than the $\beta = 0.9$ model. We see that a time varying dark energy component shifts the position of the peaks to smaller ℓ, which enhances the amplitudes of the first peaks. This effect is more evident in the model with $\beta = 0.5$. This shift in amplitude peaks is a result of a smaller distance to the scattering surface caused by the time evolving $w(a)$. This is because the point of last scattering occurs at a lower redshift for dynamical DE models since there is higher ρ_{de} at early times at the expense of ρ_c (flat universe) which delays matter-radiation equality and subsequently the point of decoupling. To illustrate, consider a dark energy model which has $w(a) > -1$ at some early time t_i. According to equation (1.9) this model will have higher density at time t_i compared to a model with $w = -1$.
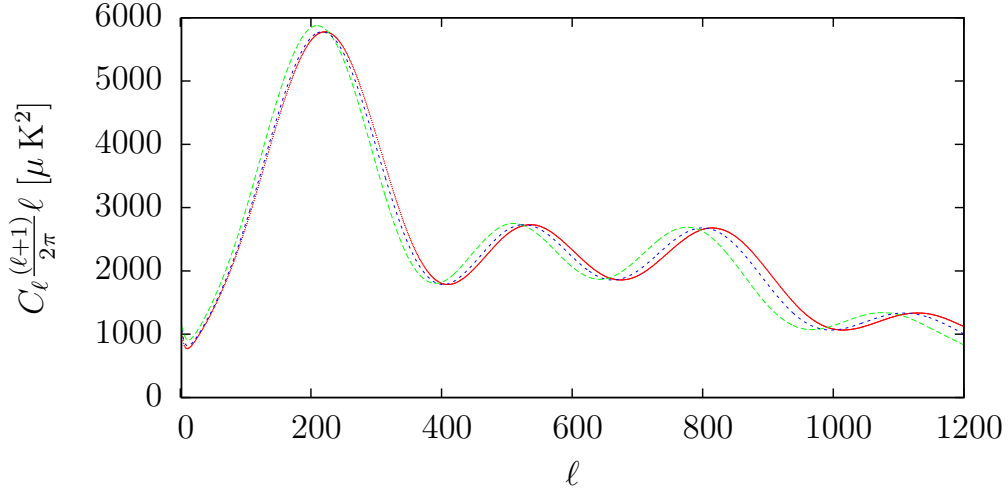
Figure 3.4: Shows the CMB spectra for the for two dynamical dark energy models described by Equation (3.27), with $\{\alpha, \beta\} = \{-1, 0.9\}, \{-1, 0.5\}$ (green,blue) and the red curve is the ΛCDM model same set of parameters except that $w(a)$ is varying the dynamical DE models. This plot was generated using CAMB [49].

3.2 The Likelihood Function

The evaluation of cosmological models in light of observational data is key in both theoretical and observational cosmology. Recent analysis is based on the likelihood function, which is a function of the parameters of a statistical model. The underlying assumption is, the likelihood of a set of parameter values given some observed outcomes is equal to the probability of those observed outcomes given those parameter values. If the distribution of the measurements that constitute the data $\mathbf{D}$ are Gaussian around their true values, then under the hypothesis ξ, the likelihood function is given by

$$L(\theta) \propto \exp\left(\frac{-\chi^2(\xi)}{2}\right),\tag{3.28}$$

where

$$\chi^2(\xi) = (\mathbf{x}(\xi) - \mathbf{D}) - (\mathbf{D} - \mathbf{x}(\xi))^T,\tag{3.29}$$

where $\mathbf{x}$ is a vector of modelled data constructed from the parameter set ξ and C is the covariance matrix of the data.

Chapter 4

Chaplygin Gas Cosmology

The Chaplygin gas falls into a class of models called Quartessence, which attempt to find a single cosmic fluid that could give rise to both dark matter and dark energy. In this section we discuss the idea of unifying dark matter and energy. We start by introducing ideas behind Quartessence, we then look at possible models that attempt this unification. Finally we study the variable Chaplygin gas and describe the equations that govern its time evolution.

4.1 Quartessence: DM/DE unification

The lack of direct detection of the dark matter particles opens the door to the possibility that both dark matter and dark energy are manifestations of the same cosmic fluid. The idea is that some perturbations in the fluid evolve into a non-linear regime to form gravitational condensates that behave as CDM in the concordance model, while the uncondensed fluid plays the role of dark energy at later times. Quartessence also provides a natural solution to the coincidence problem. The most promising models of quartessence are the so-called k-essence [36, 37] models, which are scalar field theories described by a generally covariant and Lorentz invariant action with non-canonical kinetic terms. Concerns about k-essence perturbations violating causality were raised [35] upon discovery that k-essence requires superluminal sound speed propagation in order to solve the coincidence problem. However it was later demonstrated that superluminal sound speed propagation in k-essence models does not necessarily lead to causality violation [33, 38].
Quartessence models still however face the challenge of a non-vanishing sound speed. A fluid with a non-zero sound speed has a characteristic scale below which the pressure effectively opposes gravity. The implication is that perturbations of scales below the sonic horizon will be prevented from growing. Essentially this follows from the adiabatic speed of sound [12]

$$c_s^2 = \left[\frac{\partial p}{\partial \rho}\right]_{\text{constant entropy}}, \tag{4.1}$$

where p is the pressure and ρ the energy density. The associated comoving acoustic horizon is

$$d_s = \int dt \frac{c_s}{a}, \tag{4.2}$$

where a is the scale factor. Perturbations whose comoving size R is larger than d_s grow as δ. Once the perturbations enter the sonic horizon, i.e., $R < d_s$, they undergo damped oscillations and eventually die out [19]. This effect can be studied for small ($\delta \ll 1$) perturbations using the linear theory described in section 2.1.2. However, we need to study the evolution of large perturbations in order to understand the growth of large scale structure in quartessence models. Therefore since linear theory is only relevant when $\delta \ll 1$, another approach is needed to study the growth of perturbations $\delta \geq 1$ into the non-linear regime. The approach described in section 2.1.3 for a perfectly symmetric spherical perturbation is adequate to study the growth perturbations well into the non-linear regime. However, in this model, the collapse of a perturbation is indicated by $\delta(a) \to \infty$ at a finite a, while the perturbations that are prevented from growing are damped, as in the linear theory. Nevertheless, if some of the perturbations overcome the sound speed and grow into the non-linear regime the quartessence fluid grows into a two phased mixture; the condensate and uncondensed gas. These two entities will evolve differently with time, the gravitationally bound condensate will evolve like matter, while evolution of the uncondensed fluid will be governed by its equation of state.

4.2 The Chaplygin Gas

The simplest Chaplygin gas model is characterised by a perfect fluid with equation of state [19]

$$p = -\frac{A}{\rho} \tag{4.3}$$

where p is the pressure, ρ is the energy density and A is a positive constant. This equation of state is derived from the string theory Tachyon Lagrangian [26, 27]

$$\mathcal{L} = \sqrt{A(1 - X)}, \tag{4.4}$$

where

$$X = g^{\mu\nu}\varphi_{,\mu}\varphi_{,\nu} , \tag{4.5}$$

and the scalar potential φ is related to the 4-velocity u_μ, by

$$u_\mu = \frac{\varphi_{,\mu}}{\sqrt{X}}. \tag{4.6}$$

The Chaplygin gas has been studied extensively because of its unique features. Using energy conservation, the evolution of the energy density of the Chaplygin gas, as a function of the scale factor a, is

$$\rho(a) = \sqrt{A + \frac{B}{a^6}} \tag{4.7}$$

where B is a positive integration constant. It is evident from (4.7) that at early times ($a \ll 1$), $\rho(a) \propto \sqrt{B}/a^3$, meaning that the Chaplygin gas behaves like CDM. At later times $a \simeq 1$, $\rho(a) \propto \sqrt{A + B}$ =constant, like in the case of the cosmological constant. This gas smoothly interpolates between DM and DE domination

phases. The Chaplygin gas behaves like dark matter at early times, during these early times some of the Chaplygin gas grows into the deeply non-linear regime to form a gravitationally bound condensate; we shall refer to the fraction of the VCG that collapses to form structure as the *collapsed fraction*. The evolution of the un-collapsed Chaplygin gas is governed by equation (4.3). The energy density of this uncollapsed Chaplygin gas approaches a constant at later times and brings about accelerated expansion.

The collapsed fraction depends on the Chaplygin gas sound speed. It was shown in [19] that, in order for the Chaplygin gas to fit the CMB data, about 93% percent of the Chaplygin gas has to collapse, but they also showed that less than 1% of the Chaplygin gas collapses. Therefore the Chaplygin gas has been ruled out as a viable cosmology due to retarded structure formation. To illustrate: the acoustic horizon for the Chaplygin gas is [12]

$$ds \sim \frac{a^{7/2}}{H_0}. \tag{4.8}$$

During the epoch of structure formation, $z \sim 10$ or $a \sim 0.1$, the acoustic horizon is of order 10 Mpc, which is much bigger than typical perturbation size at these early times. Therefore, since perturbations of scale less than the acoustic horizon are damped, the formation of structure is prevented by the large acoustic horizon. Furthermore, even models where the Chaplygin gas is mixed with CDM [22, 23, 24] and only plays the role of DE have been ruled out in light of SNIa data [24] and lensing statics [22, 23].

4.2.1   The Generalised Chaplygin Gas

A more 'general' form of the Chaplygin gas, the so-called generalised Chaplygin gas (GCG) [39], has been proposed. The generalised Chaplygin gas is defined by the equation of state

$$p = -\frac{A}{\rho^\alpha} \tag{4.9}$$

with $1 \geq \alpha \geq 0$ for stability and causality [32]. The additional parameter α, affords greater flexibility, and can be fine-tuned to enhance structure formation. For example, for small α, it was shown in [12] that the acoustic horizon is given by

$$ds \sim \frac{\sqrt{\alpha}a^2}{H_0}. \tag{4.10}$$

Therefore, in the context of a fine-tuned value of α, the sound horizon can be low enough to allow for sufficient collapse. In fact, it was shown that when $\alpha < 10^{-5}$ the GCG is consistent with CMB and SNIa data [48].

In references [21, 48] it is shown that the case where the GCG is mixed with CDM, and only plays the role of DE, is only consistent with SNIa and CMB data in the limit $\alpha \to 0$. In this limit however, the GCG behaves like Λ for all a. Furthermore, the analysis of [40, 41, 20] demonstrated that the SNIa data favours the case $\alpha \geq 1$, which was shown [32] to violate causality.

4.2.2 The Variable Chaplygin Gas

Another version of the Chaplygin gas model which has been proposed to address the structure formation difficulties in the standard Chaplygin gas is the *Variable Chaplygin Gas* (VCG), which replaces the constant A in the SCG by a potential $V(\varphi(a))$, where the scalar field φ, is dependent on the scale factor. The pressure is related to the density as follows:

$$p = -\frac{V_n^2(\varphi^{2n})^2}{\rho} \tag{4.11}$$

where $n \geq 0$, is a free parameter. This version of the Chaplygin gas maintains the properties of the SCG, that is, it behaves like dark matter at early times, then smoothly evolves to behave like dark energy later on. The VCG has an acoustic horizon

$$ds \sim \frac{a^{(7/2+3n)}}{H_0}. \tag{4.12}$$

The extra parameter n allows for much smaller acoustic horizon, enhancing structure formation. At redshift $z = 10$, $ds \sim$kpc, which is low enough to allow for structure formation. In fact, compared to SCG, the VCG enhances structure formation by two orders of magnitude [12]. Furthermore, it has been shown [12] that about 73% of the VCG can collapse into a gravitationally bound structure. In reference [13] it has also been shown that the VCG is compatible with SNIa observations. Both the VCG and the GCG attempt to address the structure formation problem of the Chaplygin gas, however unlike in the case of the SCG, the Lagrangian associated with the GCG has no equivalent brane interpretation [12].

The VCG is derived from the more general Tachyon Lagrangian, of which the Born-Infeld Lagrangian (Equation (4.4)) is a special case. Consider the embedding of a $(3 + 1)$-dimensional brane in a $(4 + 1)$-dimensional bulk described by coordinates $x^M = (x^\mu, x^4)$, where the index μ runs over 0, 1, 2, 3. The Tachyon Lagrangian is defined as

$$\mathcal{L} = -V(\varphi)\sqrt{1 - X}, \tag{4.13}$$

where X is defined by equation (4.5) and $\varphi(x^\mu)$ is a scalar field describing the embedding of the brane into the bulk. The pressure and energy density are defined as [12]

$$p = \mathcal{L}(\varphi, X), \tag{4.14}$$
$$\rho = 2X\mathcal{L}_X(\varphi, X) - \mathcal{L}(\varphi, X). \tag{4.15}$$

For hydrostatic equilibrium the adiabatic speed of sound $c_s^2 \geq 0$, while causality requires $c_s^2 \leq 1$. The scalar field φ and the function X are given by [12]

$$\dot{\varphi}^2 = X(\varphi, \rho), \tag{4.16}$$

and

$$X(\varphi, \rho) = \exp\left(2\int \frac{c_s^2 d\rho}{\rho + p}\right), \tag{4.17}$$

while the evolution of the energy density ρ, is given by the continuity equation

$$\dot{\rho} + 3H(\rho + p) = 0 \,. \tag{4.18}$$

It has been shown [12] that the adiabatic speed of sound

$$c_s^2 = \left[\frac{\partial p}{\partial \rho}\right]_{s/n} = \left[\frac{\partial p}{\partial \rho}\right]_{\varphi} \tag{4.19}$$

coincides with the effective speed of sound

$$\tilde{c}_s^2 = \frac{p_X}{\rho_X}, \tag{4.20}$$

that is,

$$c_s^2 = \tilde{c}_s^2$$
$$\left[\frac{\partial p}{\partial \rho}\right]_{\varphi} = \frac{p_X}{\rho_X}. \tag{4.21}$$

Violating the strong energy condition with positive ρ requires $p < 0$, while stability demands the adiabatic sound speed to be positive. These criteria are met by [12]

$$p = -\frac{A(\varphi)}{\rho^\alpha}, \tag{4.22}$$

where

$$A(\varphi) > 0, \tag{4.23}$$

and since the adiabatic speed of sound coincides with the effective speed of sound, we have

$$c_s^2 = \frac{\partial p}{\partial \rho} = \frac{\alpha A(\varphi)}{\rho^{\alpha+1}} \geq 0, \tag{4.24}$$

which requires $\alpha \geq 0$. Now when the null energy condition,

$$p + \rho = 0, \tag{4.25}$$

is saturated, i.e., when $A(\varphi) = \rho^{\alpha+1}$ it is evident from (4.24) that only for $\alpha = 1$ does $c_s^2 = 1$ when the null energy condition is saturated. Therefore, the equation of state arising from the Born-Infeld Lagrangian (4.13), which is consistent with causality and stability, is

$$p = -\frac{V(\varphi)^2}{\rho}, \tag{4.26}$$

where $V(\varphi)^2 = A(\varphi)$ is chosen to ensure condition (4.23).

From (4.17) and (4.24) we have

$$\begin{aligned} X(\varphi, \rho) &= \exp\left[2A(\varphi)\int\frac{d\rho}{\rho^3 + A(\varphi)\rho}\right] \\ &= \exp\left[-4\ln(\rho) + 2\ln(\rho - A(\varphi))\right] \\ &= \frac{\rho^2 - A(\varphi)}{\rho^2} \\ &= 1 - \frac{A(\varphi)}{\rho^2}. \end{aligned} \tag{4.27}$$

The equation of state parameter, w, for the VCG is then given by

$$w = \frac{p}{\rho} = -\frac{-V^2(\varphi)}{\rho^2} = 1 + X = -c_s^2 \tag{4.28}$$

$$p = -\frac{V_n^2 \varphi^{2n}}{\rho} \tag{4.29}$$

4.3 Variable Chaplygin Gas Evolution

Now that we have the equation of state, we need to model the growth of inhomogeneities in the VCG. Assuming that the VCG inhomogeneities are spherically symmetric, we may use the spherical model described in section 2.1.3,

$$\frac{db}{dt} - NbH = 0 \tag{4.30}$$

$$\frac{d\rho}{dt} + 3NH(\rho + p) = 0 \tag{4.31}$$

$$\frac{dH}{dt} + N\left[H^2 + \frac{4\pi G}{3}(\rho + 3p) - \frac{c_s^2\,\delta\bar{\rho}}{b^2 R^2(\rho + p)}\right] = 0. \tag{4.32}$$

where b is the local expansion scale, N is the local lapse function and $\delta = \delta(a)$ is the density contrast given by

$$\delta(a) = \frac{\rho(a) - \bar{\rho}(a)}{\bar{\rho}(a)} \,. \tag{4.33}$$

This set of coupled differential equations may be supplemented by a similar set of equations for the background evolution:

$$\frac{d\bar{\rho}}{dt} + 3\bar{H}(\bar{\rho} + \bar{p}) = 0, \tag{4.34}$$

$$\frac{d\bar{H}}{dt} + \bar{H}^2 + \frac{4\pi G}{3}\bar{H}(\bar{\rho} + 3\bar{p}) = 0, \tag{4.35}$$

where $\bar{p} = p(\bar{\rho}, \bar{\varphi})$. In k-essence, the field φ in comoving co-ordinates is a function of time only[36] which leads to,

$$\left(\frac{d\varphi}{dt}\right)^2 = N^2 X(\varphi, \rho) \,. \tag{4.36}$$

In the asymptotic region, $r \to \infty$, φ is given by

$$\left(\frac{d\varphi}{dt}\right)^2 = X(\varphi, \bar{\rho}) \,. \tag{4.37}$$

Equating (4.36) with (4.37) leads to an expression for N in terms of X

$$N = \sqrt{X(\varphi, \bar{\rho})}/X(\varphi, \rho) \,. \tag{4.38}$$

The set of coupled differential equations (4.30)-(4.37) describes both the evolution of the spherical inhomogeneity and the background. To express the evolution of the background in terms of the scale factor a we use the definition of the scale factor

$$H = \frac{1}{a}\frac{da}{dt} \,,\tag{4.39}$$

implying

$$\frac{d}{dt} \rightarrow \frac{d}{da}\frac{da}{dt} = \frac{d}{da}Ha \,.\tag{4.40}$$

The next chapter describes how these evolutions equations (Equations (4.30)- (4.37)) may be solved, for some initial conditions, to determine the evolution of the background and the inhomogeneous evolution in VCG cosmology.

Chapter 5

Methodology

The aim of this work is to determine whether the VCG is a viable alternate cosmology to the concordance model. In order to do so, we need to assess whether the VCG provides an adequate fit to current cosmological data. In this dissertation, we assume that universe evolves in a standard way until the point of decoupling, when the universe becomes transparent, i.e., photons can free stream. This point occurs at a redshift of $z_{dec} \simeq 1088.2$ [45]. During this early epoch the VCG behaves like dark matter with its equation of state parameter in the limit $w(a) \to 0$; its effective pressure approaches zero.

To get an initial estimate of the VCG cosmological parameters at decoupling, we consider a ΛCDM cosmology with the WMAP-9yr best fit parameters [45]: $H_0 = 70.0 \pm 2.2$ km s^{-1} Mpc^{-1}, $\Omega_{c,0} = 0.233 \pm 0.023$, $\Omega_{b,0} = 0.0463 \pm 0.0024$, $\Omega_{m,0} = 0.279 \pm 0.025$, $\Omega_{\Lambda} = 0.721 \pm 0.025$. Recalling the evolution of matter with scale factor, $\rho \propto a^{-3}$, the matter density parameter at decoupling may be estimated as

$$
\begin{aligned}
\Omega_m(a_{dec}) &= \frac{\Omega_{m,0}}{a_{dec}^3} \\
&\simeq 1.
\end{aligned} \tag{5.1}
$$

The second equality follows, since the universe is matter-dominated at decoupling. Therefore at decoupling,

$$
\bar{\rho}_{cr}(a_{dec}) \simeq \frac{\rho_{m,0}}{a_{dec}^3} = \rho_{cr,0} \frac{\Omega_{m,0}}{a_{dec}^3} \tag{5.2}
$$

$$
\begin{aligned}
\bar{H}(a_{dec}) &= \sqrt{\frac{8\pi G}{3} \bar{\rho}_{cr}(a_{dec})} \\
&= \sqrt{\frac{8\pi G}{3} \rho_{cr,0} \frac{\Omega_{m,0}}{a_{dec}^3}} \\
&= H_0 \sqrt{\frac{\Omega_m}{a_{dec}^3}} \tag{5.3}
\end{aligned}
$$

$$
a_{dec} = \frac{1}{1 + z_{dec}} = \frac{1}{1 + 1088.2}. \tag{5.4}
$$

Assuming $\varphi(a_{dec}) = 0$, equations (5.2)-(5.3) may be used as initial conditions for the background evolution. Then, assuming a tiny initial perturbation δ_{in}, the initial conditions for the inhomogeneity evolution are:

$$\rho_{cr}(a_{dec}) = \bar{\rho}_{cr}(a_{dec}) \left[1 + \delta_{in}\right] \tag{5.5}$$

$$H(a_{dec}) = \bar{H}(a_{dec}) \left(1 + \frac{\delta_{in}}{3}\right) \tag{5.6}$$

$$b_{dec} = a_{dec}. \tag{5.7}$$

These initial conditions for the inhomogeneity complete the set of initial conditions to evolve the inhomogeneous VCG model described by equations (4.30)-(4.37). As can be seen from equations (5.2)-(5.7), the parameter $\bar{\rho}_{cr}(a_{dec})$ dictates the VCG model initial conditions; from this point, we refer to $\bar{\rho}_{cr}(a_{dec})$ as ρ_{dec}. In fact we will see in the next chapter that, for a given n, the VCG model evolution is determined by the choice of the parameters ρ_{dec} and V_n. The n and the V_n in question are the VCG parameters in equation (4.29).

The set of coupled differential equations (4.30)-(4.37) may be solved numerically to obtain the evolution of the VCG universe. The first step in this process requires the solution to equations (4.30)-(4.37). These equations form a set of coupled differential equations which we solve numerically in FORTRAN 90 using the Runge-Kutta-Cashkarp (rk5ck) method, using the initial conditions described above. This numerical solution gives the evolution of $\bar{\rho}(a)$, $\rho(a)$, $\bar{H}(a)$, $H(a)$, $b(a)$ and $\varphi(a)$. Ideally one would use these solutions to obtain the density fluctuations in the VCG as a function of redshift and compute the corresponding transfer function describing the growth of these perturbations as a function of scale. Assuming an initial spectrum of primordial perturbations, one would then construct the power spectrum of the VCG model and compare it to the observational data. However, the calculation of the transfer function is beyond the scope of this dissertation. The reason for this is that equations (4.30)-(4.32) are for a completely spherically symmetric model, and as stated previously, collapse in this model is indicated by a diverging density contrast at finite a. Nevertheless, to reiterate a point made in the previous section; the fraction of the VCG that evolves into the deeply non-linear regime remains as a gravitationally bound condensate, rendering its effective pressure negligible. This collapsed fraction of the VCG behaves as CDM throughout the evolution of the universe. Therefore, assuming that this CDM like condensate dominates VCG model critical density at early times, we may approximate its transfer function with that of CDM. This is a reasonable approximation, recalling that in comparison to the SCG condensate formation is enhanced by two orders of magnitude. In fact it has been shown; [12], that this condensate fraction may be as high as 70% and we will show later that, with the right choice of V_n and ρ_{dec}, the VCG condensate may be as high as 80%. In fact, a damped large scale perturbation will behave as CDM right up until it starts to change to a more dark energy like behaviour, which depending on the size and sign of the perturbation can be quite late, $a \sim 0.3$. Thus the approximation to use a CDM transfer function to describe the growth of perturbations in the VCG condensate is reasonable until relatively late times. Furthermore we do not expect the CDM transfer function to have a huge impact on the observed CMB spectrum. Since the goal of this dissertation is to study the

effect of the VCG on the CMB spectrum this approximation is reasonable. It will however affect the ISW effect, since this effect affects the CMB spectrum at late times. This will be investigated in future work.

5.1 VCG Cosmic Budget

In this section we discuss the components making our VCG cosmology. Firstly we use the Press-Schechter formalism (Section 2.1.4) to calculate the fraction of the VCG that evolves into the deeply non-linear regime to form a gravitationally bound condensate. At this point, our model consists of two constituents: the gravitationally bound condensate and VCG that does not collapse and plays the role of dark energy at late times. Then we present the VCG cosmological parameters. Finally we provide a description of the numerical calculations used to study the evolution of the background and inhomogeneity (Equations (4.30)-(4.37)). We evolve these components forward in time and compute their relative energy densities today. These values will be part of the set of cosmological parameters which describe our cosmological model and will be used to compute the CMB spectrum.

5.1.1 The Condensate

We need to estimate the fraction of the VCG that collapses to form the gravitationally bound condensate. There exits an initial density contrast $\delta(a_{in}, R) = \delta_c(R)$ on a given scale, R, below which density perturbations are damped and above which the perturbations grow into the non-linear regime to form a gravitationally bound condensate [19]. This threshold initial density may be found by tracking the evolution of the the density contrast $\delta(a)$, using equations (4.34)- (4.37). Figure 5.1 illustrates the evolution of two initial perturbations from decoupling for $R = 10$kpc, $n = 2$. As stated previously a diverging $\delta(a)$ at a finite a signals collapse while a damply oscillating $\delta(a)$ indicates a perturbation that does not collapse. The green curve represents collapsing perturbation while the red curve represents a damped perturbation.

In contrast to linear theory where all initial perturbations will eventually grow into the non-linear regime to form a gravitationally bound condensate, in the case of the Chaplygin gas, perturbations with $\delta(R, a_{in}) \geq \delta_c(R)$ will grow into a non-linear gravitational condensate that remains a condensate even at low redshift. To locate this threshold $\delta_c(R)$, which at given scale separates these two regimes we use a bisection method– For each scale, we first define minimum and maximum values, δ_{in}^{min}, δ_{in}^{max}, starting from an arbitrary $\delta(a_{in})$ we track its evolution $\delta(a)$. If $\delta(a)$ diverges we assign this initial value to be δ_{in}^{max}, but if $\delta(a)$ is damped (see Figure 5.1) then we assign it to be δ_{in}^{min} and redo the calculation starting with $\delta_{in} = (\delta_{in}^{max} - \delta_{in}^{min})/2$. This process is repeated until δ_{in}^{max} are δ_{in}^{min} 'indistinguishable'. Figure 5.2 shows how this threshold initial density contrast varies with scale. For each n, the region below each curve (thin) represents the regime where the fluctuations are damped, while the region above the curves represent the region where the fluctuations grow into the deeply non-linear regime, i.e., $\delta \rightarrow \infty$. $\sigma(R)$ (thick) is the variance in density fluctuations on a given scale R, calculated from
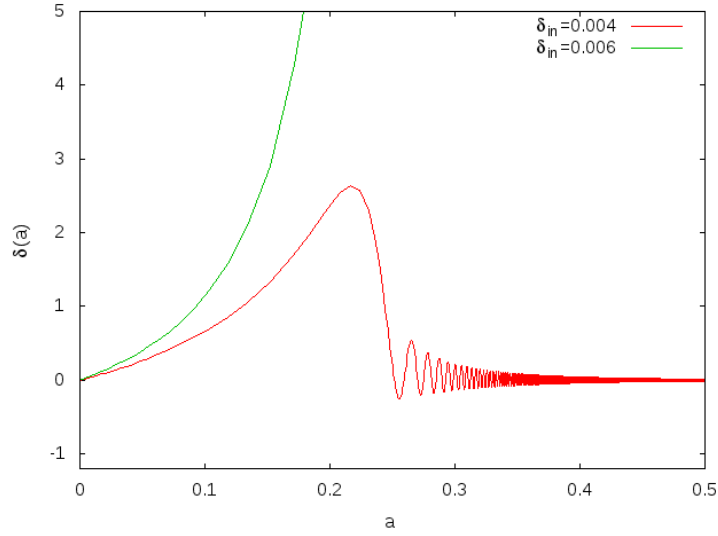
Figure 5.1: Evolution of $\delta_R(a)$ for a spherical inhomogeneity from $a_{\text{dec}} = 1/1089.2$ for $n = 2$, $R = 10$ kpc. $\delta_R^{in}(a_{\text{dec}})$ =0.004 (red) falls in the regime suffering from retarded structure formation, and undergoes damped oscillations. $\delta_R^{in}(a_{\text{dec}})$ =0.006 (green) falls into the regime where $\delta(a) \to \infty$ signalling the formation of bound structure.

the concordance model. Figure 5.2 is generated by finding the threshold $\delta_c(R)$ for various R ($10^{-3} \leq R \leq 10^3$).
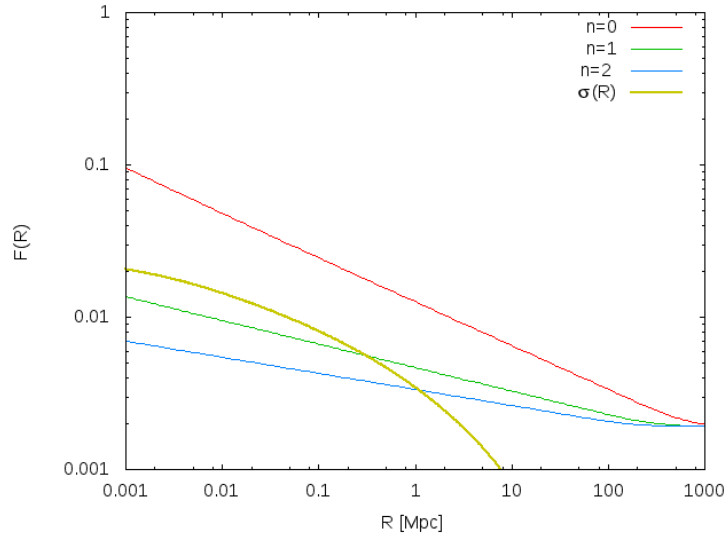

Figure 5.2: Shows how the threshold $\delta_c(R)$ separates the condensation regime from the damped oscillation regime for $n = 0, 1, 2$; the blue, green and red curves. The region below each curve (thin) represents the regime where the fluctuations are damped, while the region above the curves represent the region where the fluctuations grow into the deeply non-linear regime, i.e., $\delta \to \infty$. $\sigma(R)$ (thick) is the variance in density fluctuations on a given scale R, calculated from the concordance model

The next step is to determine the fraction of the VCG that collapses into a

gravitationally bound condensate, i.e, that falls into the regime above $\delta_c(R)$. To calculate this fraction we shall use the Press-Schechter procedure (Section 2.1.4). Assuming $\delta_c(R)$ is given by a Gaussian random field with dispersion $\sigma(R)$, the collapse fraction at a scale R is then given by equation (2.47) [12], where $\delta_c(R)$ is the threshold that divides the two above mentioned regimes at a comoving scale R and $\sigma(R)$ is the dispersion calculated using the Gaussian window function of the variance concordance model, given by

$$\sigma(R) = \int_0^{} \frac{dk}{k} \exp\left(-k^2 R^2\right) \Delta^2(k, a_{in}),\tag{5.8}$$

where

$$\Delta^2(k, a) = 7.11 \times 10^{-9} \left(\frac{k}{aH}\right)^4 T^2(k) \left(\frac{k}{7.5 a_0 H_0}\right)^{1-n_s}.\tag{5.9}$$
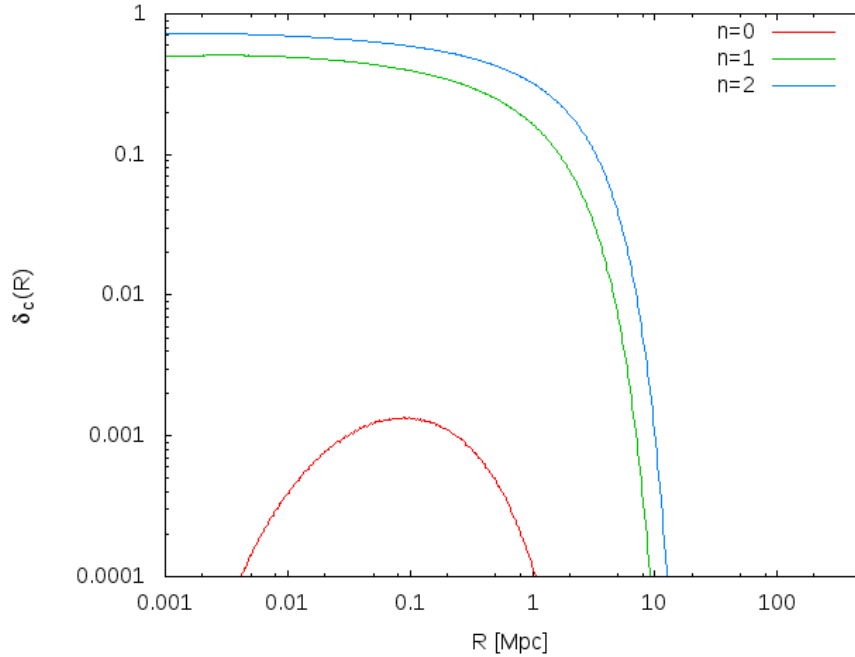

Figure 5.3: Shows the fraction of the collapsed objects using $\sigma(R)$ and $\delta_c(R)$ from Figure 5.2. The highest point of the curve $F(R)$, which occurs on small scales, is taken to be the collapse fraction on all scales.

As stated previously, we will approximate the VCG transfer function with that of CDM. Assuming such a transfer function, [34], the parameters H_0, a_0 may be fixed by fitting equation (5.9) to the SDSS data [44] and we use the WMAP-9yr data values for the spectral index $n_s = 1.0$ and $\Omega_{b,0} = 0.0499$. The fraction of the perturbations that forms a gravitationally bound condensate may then be obtained through equation (2.47) (see Figure 5.3); The integration in equation (5.8) required to find $F(R)$ is done numerically using the trapezoidal rule, $F(R)$ (Equation (2.47)) is then found using the FORTRAN 90 function $erfc$, the value of f_c is simply found by locating the peak of the $F(R)$ function, which calculates the complimentary error function. The peak of this curve, which occurs on small scales, is taken to be the

collapse fraction on all scales. That is, we are approximating the fraction of VCG that collapses on larger scales to be that which we calculated on smaller scales. This is a reasonable approximation considering that the larger scale perturbations will generally also contain smaller scale perturbations. Even though a pure Gaussian large scale perturbation might have a high δ_c, it will in general contain smaller scale perturbations within it which will collapse sooner - forming CDM like clumps within the larger scale perturbation. These CDM like clumps will assist the larger scale perturbations to collapse for a smaller δ_c than the pure Gaussian perturbations would suggest. This is because the collapsed smaller scale perturbations will behave effectively like CDM, by adding to the gravity but not the pressure of the rest of the VCG in the large scale perturbation.

Our results show that about 74%, 47% and 1% of the VCG forms gravitationally bound condensates for $n = 0$, 1, 2 respectively, these results are in agreement with [12]. Now having the fraction of the VCG that will collapse to form and remain as condensate, we now proceed to describe its evolution.

Taking f_c to be the collapsed fraction, the density ρ_{cn}, of VCG component that grows into the deeply non-linear regime, forming gravitationally bound condensate is

$$\rho_{cn}(a) = f_c \times \rho(a), \tag{5.10}$$

where $\rho(a)$ is the energy density of the VCG, which we obtain from solving the system of coupled differential equations (4.34)- (4.37). As stated previously, we fix this fraction of the VCG, ρ_{cn} as

$$\rho_{cn} = f_c \left(\frac{a_{dec}}{a}\right)^3 \rho(a_{dec}), \tag{5.11}$$

where $\rho(a_{dec})$ is the density of the VCG at decoupling.

5.1.2   The effective VCG Component

The rest of the VCG behaves as matter at early times but then tends to behave more and more like dark energy at later times. This behaviour may be seen by looking at how the VCG equation of state parameter w evolves with time. Figure 5.4 shows how the VCG transitions from behaving like matter ($w = 0$) to behaving like dark energy ($w = -1$) as a function of scale factor. This plot is generated using equations (4.28) and (4.29), where φ and ρ are found using the numerical solution described earlier in this chapter..
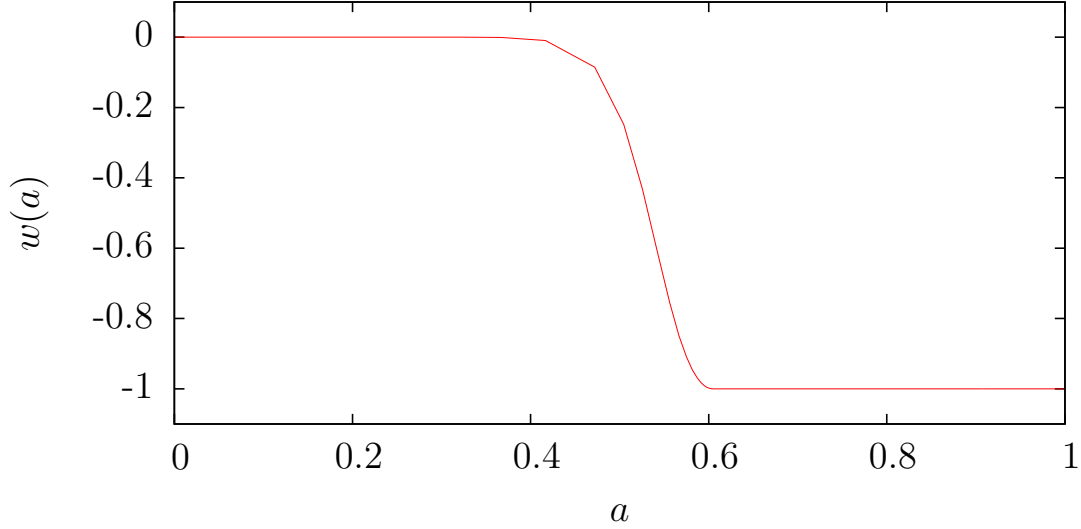
Figure 5.4: Shows the evolution of the VCG equation of state parameter w as a function of scale factor for $n = 2$. $w(a)$ transitions from behaving like matter ($w = 0$) to behaving like dark energy ($w = -1$).

The fraction of the VCG that collapses is f_c. Therefore the energy density of the fraction of the VCG that has pressure given by equation (4.29) is

$$\rho_{vcg}(a) = (1 - f_c)\rho(a). \tag{5.12}$$

The equation of state parameter for this component is given by equation (4.28).

5.1.3 A VCG Cosmological Model

In this section we formulate our VCG cosmological model. The constituents of this model were described in the previous section. So far we have not discussed the baryon content in the context of the VCG model. However we have seen the crucial role they play in the generation of anisotropies in the CMB (Section 3.1.2). Therefore, we will add baryons to the energy density. The computation of the CMB spectrum is done using the Code for Anisotropies in the Microwave Background (CAMB) [49]. To compute the CMB spectrum using CAMB, we need values of the following parameters: the value of the Hubble parameter today, H_0; the contribution (today) to the critical density of the component that plays the role of CDM, and the baryon contribution. The baryon contribution to the critical density today is fixed using the current BBN estimate for $\Omega_{b,0}h^2$, i.e.,

$$\Omega_{tot} = \Omega_{b,0} + \Omega_{cn,0} + \Omega_{vcg,0} = 1. \tag{5.13}$$

To determine the Hubble parameter in our cosmology, recall that in a spatially flat universe

$$H(a) = \sqrt{\frac{8\pi G}{3}\rho_{cr}(a)}. \tag{5.14}$$

In our cosmology

$$\rho_{cr}(a) = \rho_{vcg}(a) + \rho_{cn}(a) + \rho_b(a). \tag{5.15}$$

Therefore

$$H(a) = \sqrt{\frac{8\pi G}{3}[\rho_{vcg}(a) + \rho_{cn}(a) + \rho_b(a)]}, \tag{5.16}$$

$$H_0 = \sqrt{\frac{8\pi G}{3}(\rho_{vcg,0} + \rho_{cn,0} + \rho_{b,0})}. \tag{5.17}$$

The VCG cosmic budget at $a = 1$ is made up of the following constituents:

1. **The Baryons**:
   The baryon contribution is fixed using the current BBN estimate [52]

   $$\Omega_{b,0}h^2 = 0.022 \pm 0.0022 ; \tag{5.18}$$

2. **The condensate**:
   The energy density today of the component which collapses gravitationally is given by

   $$\Omega_{cn,0} = f_c \frac{a_{dec}^3 \rho_{dec}}{\rho_{cr}} ; \tag{5.19}$$

3. **The effective VCG**:

   $$\Omega_{vcg,0} = \frac{\rho_{vcg,0}}{\rho_{cr}}. \tag{5.20}$$

This component has equation of state parameter,

$$w(a) = \frac{p_{vcg}(a)}{\rho_{vcg}(a)} = -\frac{V_n^2 \, \varphi^{16}(a)}{\rho_{vcg}^2(a)}, \tag{5.21}$$

where φ and ρ_{vcg} may be obtained from equations (4.37) and (4.34) and an initial estimate of V_n is shown in the Appendix. This component has $w = -1$ at $a = 1$ (see Figure 5.4) and can therefore account for the accelerated expansion measured using SNIa observations [13].

Chapter 6

Discussion and Results

In this chapter we study the effect of the VCG on the CMB anisotropy spectrum. In our VCG model, the VCG that collapses plays the role of CDM in structure formation, while the rest of the VCG gas brings about accelerated expansion at late times. We shall refer to this cosmology as the VCG-CDM model. The parameters of this model were presented in section 5.1.3. The evolution of the VCG that does not collapse is determined by the equation of state (5.21); from now on we denote the effective VCG equation of state parameter by $w_e(a)$. This component behaves like CDM at early times and transitions to a more dark energy like behaviour at late times. The evolution of the collapsed VCG follows that of CDM with a vanishing effective pressure.

Assuming a CDM transfer function provides a sufficient description of the VCG density perturbations, we proceed to study the validity the VCG-CDM cosmology in light of the WMAP-9yr CMB data [46].

6.1   The effects of V_n and ρ_{dec} on the collapsed fraction and $w_e(a)$

Our VCG-CDM model is characterised by two free parameters, namely the energy density of the VCG at decoupling, ρ_{dec}, and the parameter, V_n, that appears in the VCG equation of state (Equation 5.21). In this section we investigate the effect these parameters have on the collapsed fraction, f_c and the effective VCG equation of state parameter $w_e(a)$.

The Collapsed Fraction

The collapsed fraction f_c, is the fraction of the VCG that collapses into a gravitationally bound condensate, which plays the role of dark matter in structure formation. In this section we investigate the dependence of this collapse fraction on the parameters V_n and ρ_{dec}. First, to gauge the effect of V_n on f_c we vary V_n while keeping ρ_{dec} fixed. Figure 6.1a illustrates this dependence of f_c on V_n. The plots show that models with lower V_n have higher collapsed fractions, while models with higher V_n have lower collapsed fractions. This is because the amount of fluid that

collapses in a given time period depends on the pressure of the fluid. Essentially, the VCG pressure opposes gravity, retarding collapse. This VCG pressure goes as $p \propto V_n^2$, therefore increasing V_n increases the retarding influence of the pressure on gravitational collapse, leading to a lower f_c.

Similarly, we may gauge the effect of ρ_{dec} on f_c by varying ρ_{dec} at fixed V_n. Figure 6.1b shows this dependence of f_c on ρ_{dec}. The plots show that models with higher ρ_{dec} have higher collapse fractions. This is because a higher ρ_{dec} increases the critical density which leads to a higher H_0. Now since the VCG sound horizon is given by [12]

$$ds \sim \frac{a^{(7/2+3n)}}{H_0},\tag{6.1}$$

a higher H_0 results in a lower sound horizon. Now, recalling that $\delta_c(R)$ is the minimum density contrast needed to overcome the sound sound horizon, a higher ρ_{dec} will lead to a lower $\delta_c(R)$ and consequently to a larger collapsed fraction.
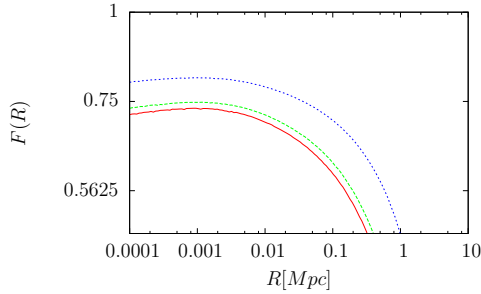

(a) Shows how V_n affects f_c, the model with the highest V_n has the lowest f_c (red) and the model with the lowest V_n has the highest f_c (blue).
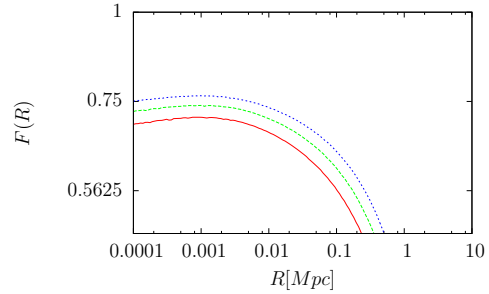
(b) Shows how ρ_{dec} affects f_c, the model with highest ρ_{dec} has the highest f_c (blue) and the model with the lowest ρ_{dec} has the lowest f_c.

The Effective VCG equation of state parameter

We now proceed to investigate the effect of V_n and ρ_{dec} on the effective VCG equation of state parameter. We start with V_n since $w_e(a)$ has an explicit dependence on this parameter (Equation (5.21)). As we have already seen, the VCG equation of state parameter transitions from $w_e(a) = 0 \rightarrow w_e(a) = -1$. We now wish to study how varying V_n affects this transition. Now, looking at the effective VCG equation of state (Equation (4.29)), we see that in the limit $V_n \rightarrow 0$, $w_e(a) \rightarrow 0$ and for large V_n, $w_e(a) \rightarrow = -1$ (Causality requires $w_e^{min} = -1$, see Equation (4.28)). Therefore, low V_n values will favour the limit $w_e(a) \rightarrow 0$ which will delay the $w_e(a) = 0 \rightarrow w_e(a) = -1$ transition to later times. Similarly, large V_n values will favour the limit $w_e(a) \rightarrow -1$ and therefore shift the transition to earlier times.
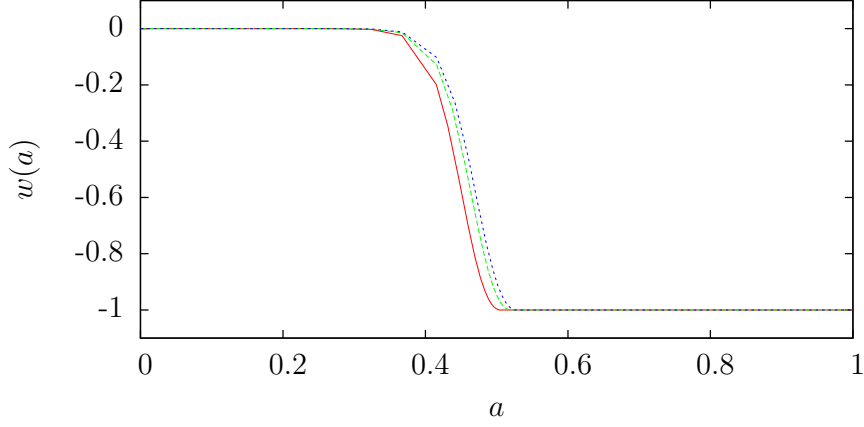
(c) Shows how V_n affects $w_e(a)$, the onset of the transition $w_e(a) = 0 \rightarrow w_e(a) = -1$ is earlier for highest V_n (red) and the onset is later for the lowest V_n (blue)
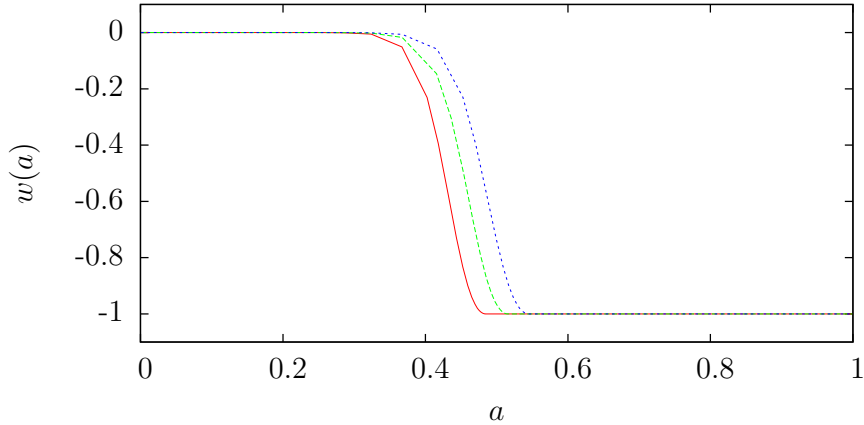
(d) Shows how ρ_{dec} affects $w_e(a)$, the onset of the transition $w_e(a) = 0 \rightarrow w_e(a) = -1$ is later for the highest ρ_{dec} (blue) and the onset earlier for the lowest ρ_{dec} (red)

This effect is illustrated in Figure 6.1c. The plot shows that in models with lower V_n, the onset of the transition $w_e(a) = 0 \rightarrow w_e(a) = -1$ is shifted to later times. Similarly, we now fix V_n and vary ρ_{dec} to study how ρ_{dec} affects $w_e(a)$. Consider the VCG equation of state,

$$p = -\frac{V(\varphi)^2}{\rho} . \tag{6.2}$$

Assuming $V(\varphi)$ remains fixed, increasing ρ will result in a smaller p. Therefore, increasing ρ will favour the limit $w = p/\rho \rightarrow 0$. Increasing ρ_{dec}, will therefore shift the onset of the transition $w_e(a) = 0 \rightarrow w_e(a) = -1$ to later times, since increasing ρ_{dec} will result in larger ρ_{vcg}. This effect is illustrated in Figure 6.1d. The plot shows that in models with a higher ρ_{dec}, the transition $w_e(a) = 0 \rightarrow w_e(a) = -1$ is onset at later times, and the onset is earlier for models with lower ρ_{dec}.

6.2   The Effect of the VCG on the CMB Spectrum

The software that we use to compute the CMB anisotropy spectra, CAMB [49], takes as input parameters the value of the Hubble parameter today, H_0, the contribution to the energy density from baryons, $\Omega_{b,0}$, the component that plays the role of dark matter, $\Omega_{dm,0}$, and the equation of state parameter $w_{de}(a)$ of the component that plays the role of dark energy; $w_{de}(a)$ may be constant or time varying. In our case $\Omega_{dm,0} = \Omega_{cn,0}$, and in the case of ΛCDM $\Omega_{dm,0} = \Omega_{c,0}$.

In section 3.1.2, considering a fiducial ΛCDM model, we saw how the components of universe affect the CMB spectrum. With that analysis in mind, we wish to gauge how f_c and $w_e(a)$ affect the parameters we will input into CAMB. These parameters are, $\Omega_{b,0}$, $\Omega_{cn,0}$ and H_0.

First lets consider f_c. Looking at equations (5.10) and (5.12), we see that increasing f_c leads to a higher ρ_{cn} to ρ_{vcg} ratio today, which results in a smaller H_0 since like CDM the VCG condensate opposes cosmic expansion. Now since we have fixed $\Omega_{b,0}h^2 = 0.022$, $\Omega_{b,0}$ will also vary as H_0 varies. To gauge the effect of $w_e(a)$ on these parameters, imagine that $w_e(a)$ approaches -1 at earlier times, then

$$\rho_{vcg} \propto \exp\left\{-3 \int^a \frac{da}{a}[1 + w_e(a\,)]\right\}$$

will give a larger ρ_{vcg} to ρ_{cn} ratio, compared to models where $w_e(a) \to -1$ at later times, which will result in higher H_0, and consequently affect $\Omega_{b,0}$.

Knowing how the VCG parameters affect the CMB spectrum, we now attempt to fit the VCG-CDM model to the WMAP-9 CMB data [46]. We use a chi-squared (χ^2) test to gauge the likelihood our model is the correct description of our universe. The χ^2 test is a special case of likelihood test described in section 3.2, and is defined by

$$\chi^2 = \sum_i^N \frac{(\xi_i^* - \xi_i)^2}{\sigma_i^2} \,, \tag{6.3}$$

where ξ_i^* are the observed frequencies, ξ_i are the predicted frequencies, σ_i is the variance in the observed frequencies and N is the number of observations. To quantify the accuracy of a model, it useful to define the χ^2 *per degrees of freedom* parameter,

$$\chi_D^2 = \frac{\chi^2}{D} \,, \tag{6.4}$$

where D, is the degrees of freedom given by $D = N - m - 1$, where N is the number of data points fitted and m is the number of free parameters of the model. In our case, we fit to 1199 WMAP-9 data points and our model has two free parameters, therefore $D = 1199 - 2 - 1 = 1196$. A good fit model is then considered to be one with $\chi_D^2 \sim 1$.

We now proceed to compare our VCG-CDM to the WMAP data. Table 6.1 shows the parameters used to construct different VCG-CDM models, in the last column are the χ_D^2 for the different models. Table 6.1a represents models in which V_n is kept constant and ρ_{dec} is allowed to vary and Table 6.1b represents models in which

ρ_{dec} is kept constant while V_n is allowed to vary. From these tables we see that models with a higher f_c have smaller χ_D^2 values compared to models with a lower f_c.

| $\tilde{V}_n$	$\tilde{\rho}_{dec}$	f_c	$\Omega_{b,0}h^2$	$\Omega_{cn,0}h^2$	$\Omega_{b,0}$	$\Omega_{cn,0}$	$\Omega_{vcg,0}$	H_0	χ_D^2
1.0000	0.7500	0.7126	0.0220	0.0682	0.0473	0.1469	0.8079	68.1652	14.16
1.0000	0.9000	0.7308	0.0220	0.0855	0.0456	0.1771	0.7793	69.4659	5.43
1.0000	1.0000	0.7405	0.0220	0.0948	0.0447	0.1926	0.7646	70.1576	5.64
1.0000	1.2000	0.7566	0.0220	0.1160	0.0428	0.2256	0.7333	71.7042	4.07
1.0000	1.3000	0.7640	0.0220	0.1275	0.0418	0.2424	0.7174	72.5295	2.65

(a)

| $\tilde{V}_n\times$	$\tilde{\rho}_{dec}\times$	f_c	$\Omega_{b,0}h^2$	$\Omega_{cn,0}h^2$	$\Omega_{b,0}$	$\Omega_{cn,0}$	$\Omega_{vcg,0}$	H_0	χ_D^2
0.5000	1.0000	0.7583	0.0220	0.0967	0.0531	0.2337	0.7159	64.3370	5.10
0.7500	1.0000	0.7482	0.0220	0.0949	0.0482	0.2078	0.7462	67.5819	5.53
0.9000	1.0000	0.7434	0.0220	0.0966	0.0458	0.2010	0.7552	69.3285	5.24
1.0000	1.0000	0.7358	0.0220	0.0946	0.0426	0.1831	0.7760	71.8615	5.64
1.2500	1.0000	0.7346	0.0220	0.0938	0.0422	0.1799	0.7796	72.1983	5.96

(b)

Table 6.1: Table showing the dependence of the VCG cosmology on the parameters V_n, ρ_{dec}. In table (a) V_n is fixed and ρ_{dec} varies, while table (b) has fixed ρ_{dec} and varying V_n. The WMAP-9 ΛCDM values are $H_0 = 70.0, \Omega_{c,0} = 0.233, \Omega_{b,0} = 0.0463$ $\Omega_\Lambda = 0.721$

Figures 6.1e and 6.1f shows the CMB spectra computed from some of the models in Table 6.1a and 6.1b respectively. In both sub-figures, the green green curve is the ΛCDM model constructed from the WMAP-9 best fit parameters and the error bars are from the WMAP-9 data [46]. Figure 6.1e represents the models in Table 6.1a, in which V_n is fixed and ρ_{dec} varies. These plots show that increasing ρ_{dec} lowers the peak amplitudes and as discussed above, this is a consequence of a higher ρ_{cn} to ρ_{vcg} ratio. Figure 6.1f represents models in Table 6.1b, in which ρ_{dec} is fixed. These plots show that increasing V_n results in higher peak amplitudes. This is a consequence of a lower ρ_{cn} to ρ_{vcg} ratio. Now recalling the analysis in section 3.1.2, higher amplitude peaks are due to a low CDM to dark energy ratio. Therefore in the case of the VCG-CDM model, we need a higher ρ_{cn} to ρ_{vcg} ratio to lower amplitude peaks. We have already seen that high ρ_{cn} to ρ_{vcg} ratios are due to high ρ_{dec} and low V_n values, this trend is also evident in Table 6.1. This ratio is also higher in models with a higher f_c. In fact looking at Figure 6.1, we see that models with a higher f_c are better fits to the WMAP data.
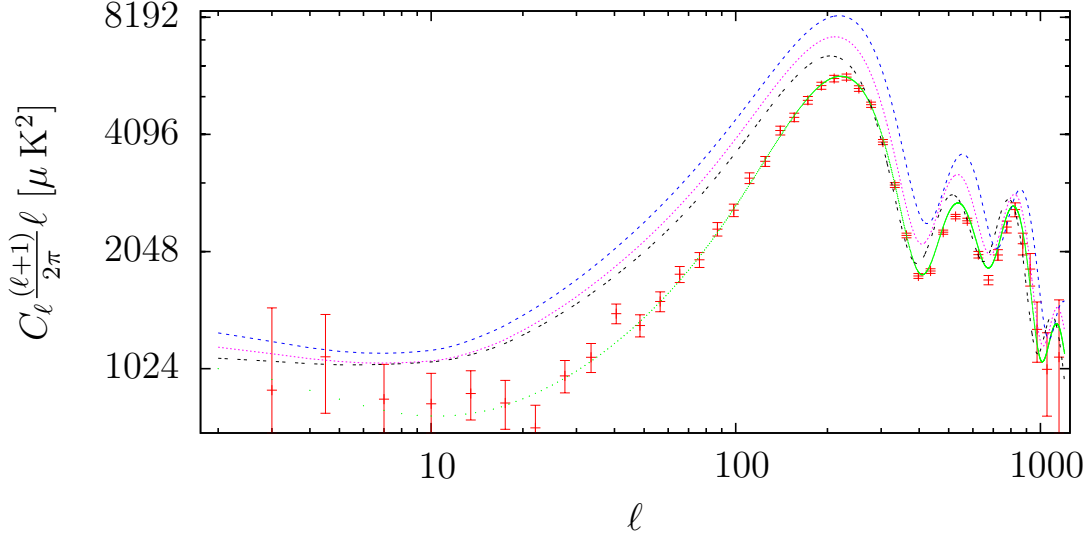
(e) Shows four VCG models taken from Table 6.1a and the WMAP-9 binned data error bars (red) [46]. The green curve represents a ΛCDM model constructed from the WMAP-9 best fit parameters [45]. $H_0 = 70.0$, $\Omega_{c,0} = 0.23$, $\Omega_{b,0} = 0.0463$. In the plots ρ_{dec} increases from $0.75\,\rho_{dec}$ to $1.3\,\rho_{dec}$ (blue-black) while V_n is kept constant.
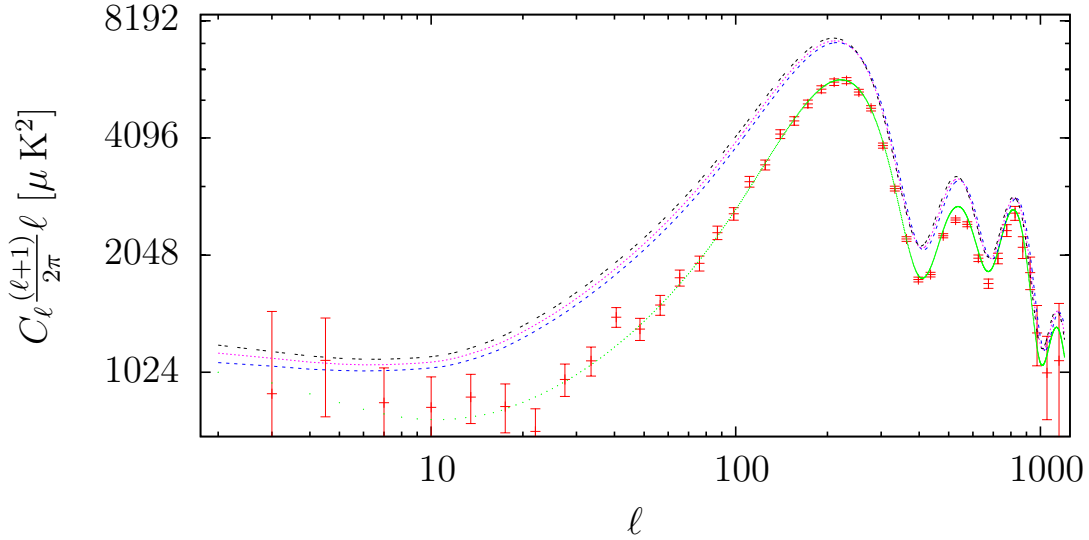
(f) Shows four VCG models taken from Table 6.1b and the WMAP-9 binned data error bars (red) [46]. The green curve represents a ΛCDM model constructed from the WMAP-9 best fit parameters [45]. $H_0 = 70.0$, $\Omega_{c,0} = 0.23$, $\Omega_{b,0} = 0.0463$. In the plots V_n increases from $0.5\,V_n$ to $1.25\,V_n$ (black-blue) while ρ_{dec} is kept constant.

Figure 6.1

We therefore search for a VCG-CDM model constructed from a combination of V_n and ρ_{dec} that give a high collapse fraction. As a prior for this model, we impose the WMAP-9 constraint, $H_0 = 70.0 \pm 2.2 \text{ km s}^{-1}\text{Mpc}^{-1}$, on this model. Different combinations of V_n and ρ_{dec} can have very high collapse fractions. However we found that high collapsing models constructed from V_n and ρ_{dec} which are too different

from the V_n and ρ_{dec} values estimated by equations (A.6) and (5.2) respectively, are not good fits to the data. We therefore restrict our search to the ranges $2.0\rho_{dec} \geq \rho_{dec} \geq 0.5\rho_{dec}$ and $1.5V_n \geq V_n \geq 0.1V_n$. We find that model that has the lowest χ_D^2 value and a high f_c is one with $V_n = 0.7V_n$ and $\rho_{dec} = 1.65\rho_{dec}$; the values are $\chi_D^2 = 2.03$ and $f_c = 80\%$. Figure 6.2 shows the spectrum for this model, we see that this model is much better fit compared to the models in Table 6.1. However, the VCG-CDM peak positions are slightly shifted towards smaller ℓ. There is also a slight disparity in the peak amplitudes relative to the ΛCDM spectrum. As we saw in section 3.1.2, a shift in peak positions is caused by a smaller distance to the last scattering surface. Indeed looking at the values of H_0 in both models we see that the VCG-CDM model has lower H_0 compared to the ΛCDM model.
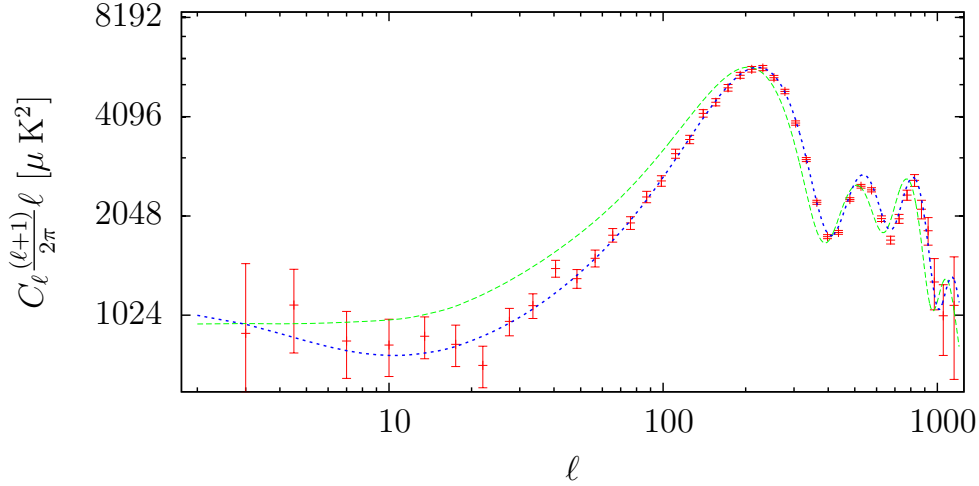

Figure 6.2: Shows a VCG-CDM model with $f_c = 0.796$, $\Omega_{b,0} = 0.0460$, $\Omega_{cn,0} = 0.341$, $\Omega_{vcg,0} = 0.615$, $H_0 = 69.17$. Also included is the WMAP-9 binned data error bars (red) [46]. The green curve represents a ΛCDM model constructed from the WMAP-9 best fit parameters [46]: $H_0 = 70.00$, $\Omega_{c,0} = 0.233$, $\Omega_{b,0} = 0.0463$.

In Figure 6.3 we show the corresponding peaks separately for a better view of the disparity in peak amplitudes between the two spectra. Also included in the plots are the WMAP-9 binned data error bars. The plots show that all the peaks of VCG-CDM spectra are lower than their corresponding ΛCDM peaks except for the first peak. Now, as previously stated, a high dark matter to dark energy ratio today leads to lower peak amplitudes. Looking at comparing these ratios for the ΛCDM ($\rho_{c,0}$ to $\rho_{\Lambda,0}$) and the VCG-CDM model ($\rho_{cn,0}$ to $\rho_{vcg,0}$) we see that the VCG-CDM ratio is higher. Indeed, looking at the respective peak amplitudes in Figure 6.3, we see that the VCG-CDM amplitudes are lower than those of ΛCDM. The enhancement of the odd peaks over the even peaks with respect to the even peaks is likely due to a lower $\Omega_{b,0} = 0.0460$ in the VCG-CDM model compared to $\Omega_{b,0} = 0.0463$ in the ΛCDM, since decreasing $\Omega_{b,0}$ lowers the the even peak amplitudes.

(a) First peak

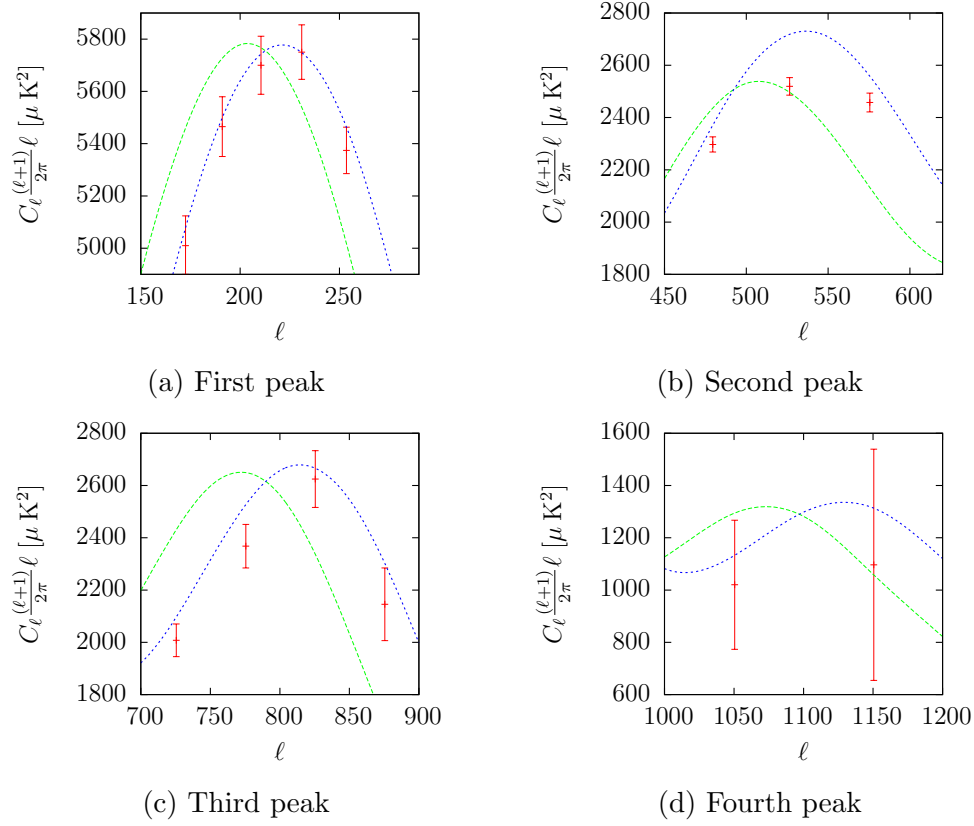(b) Second peak

(c) Third peak

(d) Fourth peak

Figure 6.3: Shows the difference in the CMB spectrum amplitudes and positions of the VCG-CDM model (green) and the ΛCDM model (blue) constructed from the WMAP-9 cosmological parameters, also included in the plots are the WMAP-9 binned data error bars (red)

Chapter 7

Summary and Conclusions

Although the concordance model has been shown to fit a wide range of observations, it is plagued by theoretical issues. These problems are naturally addressed in quartessence cosmology. However, it is important to compare these quartessence models to observational data. In this dissertation we have studied the effect of a quartessence model known as the variable chaplygin gas on the CMB anisotropy spectrum.

The main challenge of quartessence cosmology is getting a sufficient amount of the quartessence fluid to collapse via gravity to form structure. This gravitational collapse is retarded by large effective sound speeds. Indeed the simple chaplygin gas has been ruled out as a viable cosmology due to retarded structure formation. Generalisations of the chaplygin gas were subsequently proposed to address the issue of structure formation. Firstly, the generalised chaplygin gas model. This model has an extra parameter α, and through a fine-tuned value of this extra parameter this model is able to achieve the sufficient collapse to account for the observed structure. However, in the limit that the GCG accounts for the observed structure, it is equivalent to the concordance model. Secondly, the VCG has recently been proposed. Unlike the GCG the VCG avoids causality and stability violations. Bilić *et al.*[12] showed that for $n = 2$ about 70% of the VCG can grow into the non-linear regime to form gravitationally bound structure.

In this dissertation we have investigated whether it is possible to find a VCG cosmological model that can fit the current CMB data. We have done this by assuming that a CDM transfer function provides an adequate description of the VCG density perturbations. We find that a collapse fraction is required to fit the CMB data. We have shown that for $n = 2$, this collapsed fraction can be as high as 80% for the appropriate choices of the parameters describing our VCG cosmology. Using a model in which the collapsed VCG condensate plays the role of CDM in the concordance model and the remaining uncollapsed VCG replacing dark energy, we compute the CMB power spectrum for our VCG cosmology. Our best fit VCG model (Figure6.2) has a χ^2 per degrees of freedom of 2.03 with respect to the WMAP-9yr data. However, there is slight discrepancy in peak positions and amplitudes between our model and the concordance which we have concluded is due a shorter distance to the last scattering surface and different effective dark matter to dark energy ratios and a different baryonic content respectively.

Our results are very encouraging and suggest that the viability of a VCG cosmology as an alternate concordant model warrants further investigation. In this analysis we have used the CDM transfer function as an approximation of that of the VCG condensate. However, as discussed, in fact the critical density contrast required to overcome the sound horizon of the VCG is scale dependent. A more thorough analysis would require the computation of the VCG transfer function. We hope to calculate this transfer function as an extension to this work.

Appendix A

Estimating V_n

We want to must estimate V_n. This estimation is taken from [12]. Since we want to get something that looks like ΛCDM we approximate $w(a)$ as in ΛCDM

$$X = 1 - w(a) \simeq 1 - \frac{\Omega_\Lambda}{\Omega_\Lambda + \Omega_m a^{-3}} \tag{A.1}$$

then using equation (4.37) we get

$$\frac{d\phi^2}{dt} = 1 - \frac{\Omega_\Lambda}{\Omega_\Lambda + \Omega_m a^{-3}}$$

$$\left(\frac{d\phi}{da}\right)^2 \left(\frac{da}{dt}\right) = \frac{\Omega_m a^{-3}}{\Omega_\Lambda + \Omega_m a^{-3}}$$

$$\left(\frac{d\phi}{da}\right)^2 = \frac{1}{\dot{a}^2}\left(\frac{\frac{\Omega_m a^{-3}}{\Omega_\Lambda}}{1 + \frac{\Omega_m a^{-3}}{\Omega_\Lambda}}\right)$$

$$\frac{d\varphi}{da} = \pm\frac{a^2}{\dot{a}^2}\frac{1}{a^2}\sqrt{\frac{\frac{\Omega_m a^{-3}}{\Omega_\Lambda}}{1 + \frac{\Omega_m a^{-3}}{\Omega_\Lambda}}}$$

$$= \frac{1}{H_0^2}\frac{a^{3/2}}{\sqrt{\Omega_m}}\sqrt{\frac{\frac{\Omega_m a^{-3}}{\Omega_\Lambda}}{1 + \frac{\Omega_m a^{-3}}{\Omega_\Lambda}}} \tag{A.2}$$

$$\tag{A.3}$$

$$\varphi(a) \simeq \frac{2}{3H_0\sqrt{\Omega_m}}\mathrm{ArcTan}\left(\sqrt{\frac{\Omega_\Lambda a^3}{\Omega_m}}\right). \tag{A.4}$$

Fixing the pressure given by VCG to be equal to that of Λ at $a = 1$,

$$\rho_0 = \frac{-V(\varphi)}{\rho_0} = \frac{V_n \varphi^{4n}(a=1)}{\rho_0} = \rho_0\Omega_\Lambda, \tag{A.5}$$

leading to

$$
\begin{aligned}
V_n^2 &= \frac{\rho_0^2 \Omega_\Lambda}{\varphi^{4n}(a=1)} \\
V_n &= \frac{\rho_0 \sqrt{\Omega_\Lambda}}{\varphi^{2n}(a=1)} \\
&= \frac{3\alpha_n}{8\pi G} H_0^{2n+1} \\
&= \rho_0 \alpha_n H_0^{2n}
\end{aligned}
\tag{A.6}
$$

where

$$
\alpha_n = \Omega_\Lambda \left[\frac{2}{3\sqrt{\Lambda}} \mathrm{ArcTan}\left(\sqrt{\frac{\Omega_\Lambda}{\Omega_m}} \right) \right]^{-2n}.
\tag{A.7}
$$

Bibliography

[1] A. Liddle, *An Introduction to Modern Cosmology*, New York, Wiley (1999).

[2] S. Dodelson, *Modern Cosmology*, Carlifonia, Academic Press (2003).

[3] C. Zunckel, *Beyond The Standard Cosmological Model: Dark Energy, Massive Neutrinos and Statistical Isotropy*, University of Oxford (2008)

[4] E. P. Hubble, Proc. Natl. Acad. Sci. USA **15**, 168-173

[5] W. L. Freedman *et al.*, Ap.J., **535**, 45-72 (2001)

[6] A. Coc, Ap.J., **600** 544-552 (2004)

[7] P. J. E. Peebles, 1998a, Ap.J., **325**, 17 (1998a)

[8] P. J. E. Peebles, Phys. Rev. D **37**, 3406 (1998b)

[9] Z. K. Guo *et al.*, Phys. Lett. B., **608**, 177 (2005)

[10] A. Cohen, D. Kaplan and A. Nelson, Phys. Rev. Lett., **82**, 4971 (1999)

[11] Caldwell, R., Phys. Lett. B., 545, **23** (2002)

[12] N. Bilić, G. B. Tupper and R. D. Viollier, Phys.Rev. D **80**, 023515 (2009)

[13] Z. Guo and Y. Zhang, Phys. Lett. B645:326-329, (2007)

[14] G. Sethi *et al.*, Int. J. Mod. Phys D**15**, 1089 (2006)

[15] C. Ranjit, S. Shuvendu, U. Debnath, International Journal of Theoretical Physics, **52** 3, 862-776 (2013)

[16] W.H. Press and P. Schechter, Ap.J., **187**, 425 (1974)

[17] R. K. Sheth and G. Tormen, MNRAS, **329**, 61 (2002)

[18] A. Jenkins et al., MNRAS, **321**, 372 (2001)

[19] N. Bilić, R.J. Lindebaum, G.B. Tupper, and R.D. Viollier, JCAP **0411**, 008 (2003); [arXiv: astro-ph/0307214].

[20] V. Gorini, A.Y. Kamenshchik, U. Moschella, O.F. Piattella, and A.A. Starobinsky, JCAP **0802**, 016 (2008).

[21] H.B. Sandvik, M. Tegmark, M. Zaldarriaga, and I. Waga, Phys. Rev. D **69**, 123524 (2004).

[22] A. Dev, J.S. Alcaniz, and D. Jain, Phys. Rev. D **67**, 023515 (2003).

[23] A. Dev, D. Jain, and J.S. Alcaniz, Astron. Astrophys. **417**, 847 (2004).

[24] P.P. Avelino, L.M.G. Beça, J.P.M. de Carvalho, C.J.A.P. Martins, and P. Pinto, Phys. Rev. D **67**, 023511 (2003).

[25] J.S. Alcaniz, D. Jain, and A. Dev, Phys. Rev. D **67** 043514 (2003).

[26] A. Sen, Mod. Phys. Lett. **A17**, 1797 (2002); A. Sen, J. High Energy Phys. JHEP **0204**, 048 (2002); A. Sen, J. High Energy Phys. JHEP **0207**, 065 (2002).

[27] G.W. Gibbons, Class. Quant. Grav. **20**, S321 (2003).

[28] W. Hu, *CMB Anisotrpies: A Decadal Survey. In birth and evolution of the universe: RESCEU. Universal Academy Press, Tokyo*

[29] Rauch et al., Ap.J., **489**, 7 (1997)

[30] Riess et al., Ap.J., **116**, 1009 (1998)

[31] Perlmutter et al., Ap.J., **517**, 565 (1999)

[32] G.F.R. Ellis, R. Maartens, and M.A.H. MacCallum, Gen. Relativ. Gravit. **39**, 1651 (2007).

[33] J.P. Bruneton, Phys. Rev. D **75**, 085013 (2007).

[34] J.M. Bardeen, J.R. Bond, N. Kaiser, and A.S. Szalay, Ap.J., 304, 15 (1986)

[35] C. Bonvin, C. Caprini, and R. Durrer, Phys. Rev. Lett. **97**, 081303 (2006).

[36] C. Armendariz-Picon, T. Damour, and V. Mukhanov, Phys. Lett. B **458**, 209 (1999). J.U. Kang, V. Vanchurin, and S. Winitzki, Phys. Rev. D **76**, 083511 (2007).

[37] J. Garriga and V.F. Makhanov, Phys. Lett. B **458**, 219 (1999).

[38] E. Babichev, V. Mukhanov, and A. Vikman, JHEP **0802**, 101 (2008). M.C. Bento, O. Bertolami, and A.A. Sen, Phys. Rev. D **66**, 043507 (2002). [arXiv:gr-qc/0202064].

[39] M.C. Bento, O. Bertolami, and A.A. Sen, Phys. Rev. D **66**, 043507 (2002). [arXiv:gr-qc/0202064].

[40] O. Bertolami, A.A. Sen, S. Sen, and P.T. Silva, MNRAS **353**, 329 (2004).

[41] O. Bertolami, Preprint (2004) [arXiv: astro-ph/0403310].

[42] `http://sdss.org`

[43] Sachs R.K., Wolfe A.M., Ap.J **147** 73, (1967).

[44] Ahn, Christopher P. et al., Ap.J.S, **203** 21, (2012).

[45] http://lambda.gsfc.nasa.gov/product/map/dr5/params/lcdm_wmap9.
     cfm

[46] http://lambda.gsfc.nasa.gov/data/map/dr5/dcp/spectra/wmap_
     binned_tt_spectrum_9yr_v5.txt

[47] L.R. Abramo, R.C. Batista, L. Liberato, and R. Rosenfeld, JCAP **0711** 012,
     (2007).

[48] L. Kai *et al.*, RAA **159** 13, (2013) [arXiv:1210.5021v1]

[49] A. Lewis, A. Challinor, Ap.J., **538**, (2000), [arXiv:astro-ph/991117].

[50] Seljak *et al.*, Ap.J., **469**, (1996) [astro-ph/9603033].

[51] S.D.M White *et al.*, Nature, 336, 429 (1993)

[52] G. Steigman, Int. J. Mod. Phys.,E15 (2006)

[53] Albrecht, A.,*et al.*(2006),[arXiv: astro-ph/0609591]

[54] L. Perivolaropoulos, (2008),[arXiv: astro-ph/08114684]